Research Article[1]

OsKish coordinates with Lunapark and RHD3 to maintain the structural stability of endoplasmic reticulum network in rice

Pengcheng Zhang[1, #], Yihua Wang[1, #], Yun Zhu[2, #], Yu Zhang[1], Xiaohang Han[2], Yu Chen[2], Jianing Zhang[2], Bingke Luo[2], Xiuhao Bao[1], Hongming Wu[1], Fan Wang[2], Ao Zhang[1], Cailin Lei[2], Xin Wang[2], Zhijun Cheng[2], Chao Li[1], Yuqiang Liu[1], Haiyang Wang[2], Yulong Ren[2, *], and Jianmin Wan[1,2, *]

[1]State Key Laboratory for Crop Genetics & Germplasm Enhancement and Utilization, Zhongshan Biological Breeding Laboratory, National Field Observation and Research Station (Jiangsu Nanjing) for Rice Germplasm Resources, Nanjing Agricultural University, Nanjing 210095, China.

[2]State Key Laboratory of Crop Gene Resources and Breeding, Institute of Crop Sciences, Chinese Academy of Agricultural Sciences, Beijing 100081, China.

[#]These authors contributed equally: Pengcheng Zhang, Yihua Wang, and Yun Zhu.

[*]Author for correspondence: wanjm@njau.edu.cn (J.W.); renyulong@caas.cn (Y.R.)

Abstract

The endoplasmic reticulum (ER) is the largest intracellular membrane-bound organelle in eukaryotic cells, comprising an interconnected network of tubules and sheets. Lunapark (LNP) functions as an E3 ubiquitin ligase that targets RHD3, a dynamin-like GTPase essential for homotypic fusion of ER tubules, for proteasomal degradation, thereby modulating ER

[T]he author (s) responsible for distribution of materials integral to the findings presented in this article in accordance with the policy described in the Instructions for Authors (https://academic.oup.com/plcell/pages/General-Instructions) is (are): Jianmin Wan (wanjm@njau.edu.cn).

tubule stability. However, the regulatory mechanism governing LNP activity remains largely unknown. Here, we report the characterization of the rice *oskish* mutant, which exhibits aberrant aggregation of ER tubules and defective ER exit of seed storage proteins. OsKish is an ER-localized small protein that physically interacts with both OsLNPs and RHD3-like (RHD3L) protein. OsKish stabilizes OsLNPs by suppressing their auto-ubiquitination; concomitantly, OsKish attenuates the membrane fusion activity of RHD3L possibly by inhibiting its oligomerization. Altogether, our studies propose an OsKish–OsLNPs–RHD3L framework for fine-tuning homotypic ER tubule fusion in rice, providing mechanistic insights into the maintenance of ER architecture in plants.

Introduction

The endoplasmic reticulum (ER) is the largest membrane-bound organelle in eukaryotic cells, which comprises the nuclear envelope, sheet-like cisternae, and a continuous polygonal network of tubules connected by three-way junctions (Shibata et al. 2006; Vitale and Boston 2008; Chen et al. 2012a). The ER plays diverse and important roles in the cell, including protein synthesis and quality control (Baumann and Walz 2001; Vitale and Boston 2008; Sun et al. 2021), lipid synthesis (Fagone and Jackowski 2009), and calcium homeostasis (Brandizzi 2021), while also serving as the gateway for secretory or lysosomal/vacuolar pathways (Sun et al. 2021). Live-cell imaging reveals that the ER is constantly remodeling, with continuous fusion of tubules to form cisternae and a complex polygonal network (Sparkes et al. 2011). Such dynamic structural change is important for ER function (Westrate et al. 2015). Consequently, investigating the molecular mechanisms that maintain the dynamic and intricate ER networks is crucial for understanding ER function.

Numerous studies in yeast, mammals, and higher plants have revealed a conserved and essential role of the dynamin-like GTPases atlastin (ATL), Sey1p, and RHD3 in mediating the homotypic fusion of membrane tubules to form the polygonal ER network through structures known as three-way junctions (Bian et al. 2011; Chen et al. 2011; Friedman and Voeltz 2011; Hu et al. 2011; Anwar et al. 2012; Yan et al. 2015; Shi et al. 2024). For example,

downregulating *ATL* expression results in a discontinuous and fragmented ER, whereas *ATL* overexpression impairs the normal ER network and leads to the formation of expanded cisternae (Orso et al. 2009; Liu et al. 2019). In the yeast *sey1p* mutant, ER sheets increase while branched ER tubules decrease (Chen et al. 2012b). Loss of *RHD3* function in *Arabidopsis thaliana* leads to the formation of long and unbranched ER tubules, whereas *RHD3* overexpression results in the abnormal accumulation of sheet-like ER due to excessive membrane fusion (Zhang et al. 2013; Sun et al. 2020).

In addition, it has been shown that the protein family named Lunapark (LNP), which contains a conserved "LNPARK" motif, plays a conserved role in stabilizing nascent three-way junctions by inhibiting ATL-mediated fusion (Chen et al. 2015; Kriechbaumer et al. 2018; Zhou et al. 2019; Jang et al. 2023). For instance, Arabidopsis LNP1 and LNP2 have been implicated in functioning as E3 ubiquitin ligases to mediate the degradation of RHD3, thereby maintaining a stable tubular ER network (Kriechbaumer et al. 2018; Sun et al. 2020). Moreover, a recent study showed that RTNLB3 interacts with RHD3 and inhibits its ER fusion activity by interfering, at least in part, with its oligomerization (Wang and Zheng 2024). Despite these significant advances, our understanding of the molecular mechanism underlying ATL-mediated ER membrane fusion remains limited, especially in plants. Crucial regulators modulating ER fusion are yet to be characterized to elucidate the complex network required for maintaining ER morphology in plants.

In this study, we report the identification of the rice *glutelin precursor accumulation15* (*gpa15*) mutant, which over-accumulates glutelins, a major storage protein component in rice seeds, in their precursor form in seeds and displays remarkable ER morphology defects. *GPA15* encodes a small protein, OsKish, that localizes to the ER. Interestingly, we found that OsKish interacts with OsLNPs and RHD3L, the rice homologs of LNPs and ATLs, respectively. Biochemical studies reveal that OsKish reduces the auto-ubiquitination activity of OsLNPs to prevent their proteasomal degradation. Additionally, our data suggest that OsKish modulates the homotypic ER fusion through the inhibition of RHD3L oligomerization. Taken together, our findings suggest that OsKish functions cooperatively with OsLNPs to

antagonize the fusion activity of RHD3L, providing mechanistic insights into the complex regulatory network governing homotypic ER membrane fusion in plants.

Results

The *gpa15* mutation disrupts ER morphology and impairs glutelin export from the ER.

Seed storage proteins (SSPs), such as glutelins and prolamins, are critical determinants of rice grain quality. They are synthesized co-translationally in the ER and subsequently sorted into distinct protein bodies (PBs): prolamins are deposited into PBIs through direct budding from the ER, whereas glutelins are delivered to protein storage vacuoles (PSVs) via the Golgi-dependent vacuolar trafficking pathway, ultimately forming PBIIs (Wang et al. 2016; Zhu et al. 2019; Ren et al. 2020; Bao et al. 2023). In an effort to identify key regulators governing the PSV transport pathway in rice, we identified two allelic glutelin trafficking-deficient mutants, designated *gpa15-1* and *gpa15-2* (Figure S1a). We focused on the *gpa15-1* mutant for further study given the short life cycle of its wild-type (WT) background, Kitaake. The *gpa15-1* mutant developed a macroscopically opaque and floury endosperm, in contrast to the transparent appearance of the WT endosperm (Figure S1a). Scanning electron microscopy (SEM) reveals that the *gpa15-1* endosperm consisted of loosely-arranged starch granules, in contrast to the tightly-packed polyhedral starch granules observed in the WT endosperm (Figure S1, b and c). SDS-PAGE coupled with immunoblotting reveals aberrant accumulation of glutelin precursors in *gpa15-1* (Fig. 1, a to c). Additionally, immunoblotting showed a significant increase in BiP1 and PDIL1-1 abundance in *gpa15-1* (Fig. 1, d to f), similar to previously reported *gpa* mutants with defects in either folding or ER exit of glutelins, such as *gpa4* (Wang et al. 2016). Notably, *gpa15-1* displayed a seedling-lethal phenotype with no root development during germination (Figure S1d).

Coomassie Brilliant Blue (CBB)-stained semi-thin sections reveal two canonical types of PBs in the WT: light-stained, round PBI and dark-stained, irregular PBII (Fig. 1g, left panel). In the *gpa15-1* mutant, in addition to these structural intact but reduced size of PBIs and PBIIs, a type of novel PB with a distinct texture was consistently observed; this structure is

designated herein as the compound PB (Fig. 1g, middle panel). Furthermore, numerous small protein particles aggregated into a second class of aberrant structures characterized by amorphous, densely-packed clusters (Fig. 1g, right panel). To determine the nature of these abnormal structures, immunofluorescence assays were performed using antibodies specific for glutelin acidic subunits and prolamins (Fig. 1, h to j). Distinct from the strict compartmentations in the WT, where prolamins are exclusively localized to PBI, and glutelins exclusively to PBIIs (Fig. 1h), the compound PBs in *gpa15-1 harbor* both glutelins and prolamins (Fig. 1i), whereas the large aggregated structures are predominantly enriched in prolamins (Fig. 1j). Collectively, these results suggest that the *gpa15-1* mutation impairs the proper deposition of SSPs into their respective PBs.

To investigate the origin and formation of these novel structures observed in *gpa15-1*, we visualized the subcellular compartments of developing subaleurone cells directly by transmission electron microscopy (TEM) (Fig. 2, a to e). Canonical irregular-shaped PBIIs and spherical PBIs were consistently observed in the WT (Fig. 2a), whereas several types of novel structures were found specifically in *gpa15-1* (Fig. 2, b to e). A conspicuous feature observed in *gpa15-1* was the presence of dilated ER, where protein aggregates with distinct electron densities and sizes abnormally accumulated (Fig. 2b). The compound PBs in *gpa15-1* have a large electron-dense core with several small round protein aggregates in the peripheral regions (Fig. 2c). More strikingly, large aggregates with numerous radial tubular ER branches were observed in *gpa15-1*, with spherical protein aggregates enclosed in the dilated terminal lumens of ER branches (Fig. 2d). Further observations reveal that these large structures are in fact aggregates of dense ER tubules (Fig. 2e).

Immunogold labeling confirmed that glutelin-filled PBIIs are present in both the WT and the *gpa15-1* mutant; however, PBIIs in *gpa15-1* exhibit incomplete luminal filling (Fig. 2, f and g). Consistent with the CBB-stained semi-thin sections and immunofluorescence data (Fig. 1, g and h), the compound PBs, enclosed by ER-derived membranes, harbored both glutelins and prolamins (Fig. 2h). In contrast to the discrete, membrane-bound PBIs in WT, prolamin aggregates in *gpa15-1* form small, electron-dense clusters dispersed within the ER lumen (Fig. 2, i to k). Furthermore, immunogold labeling substantiated the absence of both glutelin

and prolamin aggregates within the aberrant ER structures of *gpa15-1*, as previously indicated by CBB staining and immunofluorescence assays (Fig. 2, l to n). Taken together, these results indicate that the *gpa15* mutation disrupts both tubular ER architecture and the efficient ER exit of glutelins in rice.

GPA15 encodes a small protein that is highly conserved in eukaryotes.

Genetic analysis revealed that the mutant phenotypes were inherited as a single nuclear recessive mutation (Table S1). Using the map-based cloning strategy, we mapped the *GPA15* locus to a 506-kb physical region on chromosome 5 (Fig. 3a). Re-sequencing analysis identified single nucleotide substitutions in *Os05g0251500*, resulting in the replacement of Gly-49 with Asp in *gpa15-1* and Leu-52 with a premature stop codon in *gpa15-2* (Fig. 3b). To verify whether *Os05g0251500* is the causal gene, we introduced a 6.4-kb genomic fragment of *Os05g0251500*, spanning the coding region and its upstream and downstream regulatory sequences, into the *gpa15-1* background. All three positive transgenic lines exhibit wild-type phenotypes (Fig. 3, c to e). Furthermore, CRISPR/Cas9-mediated knockout mutants of *Os05g0251500* phenocopied *gpa15-1* (Fig. 3, f to h). In addition, we employed an inducible RNA interference (RNAi) system to generate RNAi transgenic plants of *Os05g0251500* fusing a dexamethasone (DEX)-inducible system (Gao et al. 2014). Upon DEX treatment, the transgenic lines exhibited severe growth arrest, and ultimately died (Figure S1e). RT-qPCR analysis further confirmed the relationship between the growth defect and the reduced expression of *Os05g0251500* (Figure S1f). These results collectively demonstrate that *Os05g0251500* indeed corresponds to the *GPA15* gene. Notably, *GPA15* was predicted to encode a small protein consisting of 70 amino acid residues, with two transmembrane domains (http://smart.embl-heidelberg.de/). Phylogenetic analysis showed that GPA15 belongs to the Kish (for the word small in Hungarian) family (Figure S2), which has been implicated in glioma formation in flies and humans; however, the molecular functions remain largely unknown (Wendler et al. 2010; Portela et al. 2019; Segura-Collar et al. 2020). We refer to *GPA15* as *OsKish* hereafter.

RT-qPCR analysis showed that *OsKish* is expressed in all tissues examined, including developing endosperm at different stages (Figure S1g). The rice genome contains an *OsKish* homolog, *OsKish-L*, which encodes a protein with 78.6% amino acid sequence identity to OsKish. Although *OsKish-L* exhibited extremely low expression levels compared with *OsKish* in all tissues examined (Figure S1h), its expression driven by the *OsKish* promoter rescued the *gpa15-1/oskish-1* mutant phenotypes (Figure S1, i and j), indicating a functional conservation between both *OsKish* homologs.

OsKish is an ER-localized protein that functions in maintaining the ER functional integrity and tubular ER morphology.

To determine the subcellular localization of OsKish, we transiently expressed N- or C-terminal GFP fusions of OsKish in *Nicotiana benthamiana* leaf epidermal cells. Consistent with the ER morphology defects observed in the *gpa15-1/oskish-1* mutant, confocal microscopy reveals that both fusions exhibit a reticular localization pattern similar to that of the ER (Figure S3a). We then performed colocalization analyses using fluorescent markers specific for the ER (mRFP-HDEL) and Golgi apparatus (Man1-mCherry). As anticipated, GFP-OsKish fluorescence signals showed strong overlap with the ER marker but no detectable colocalization with the Golgi marker, as quantified by Pearson's correlation coefficient analysis using the Pearson-Spearman correlation (PSC) plugin for ImageJ (Fig. 4, a and b). Furthermore, to mitigate potential artifacts arising from overexpression-induced mislocalization, we employed the weak TR2' promoter, which was previously demonstrated to drive GUS expression at approximately one-tenth the level of the CaMV 35S promoter in leaf tissue (Bottanelli et al. 2012). Under the control of the TR2' promoter, both GFP-OsKish and OsKish-GFP fusions retain the same reticular ER-associated pattern (Figure S3b).

Several small regulatory proteins, such as WeiTsing (WTS), have been shown to function through oligomerization (Wang et al. 2023); we therefore investigated whether OsKish exhibits similar behavior. Bimolecular fluorescence complementation (BiFC) assays showed that OsKish physically interacts with itself, predominantly localized at three-way

junctions of ER, and also on ER tubules (Figure S3c). This self-interaction was further verified by the firefly luciferase complementation imaging (LCI) assay (Figure S3d). Moreover, an *in vivo* co-immunoprecipitation (Co-IP) assay showed that Flag-OsKish could be co-immunoprecipitated specifically by GFP-OsKish (Figure S3e). Taken together, these data suggest that OsKish functions as a homodimer or high-order oligomer on the ER membrane.

We next employed the DEX-inducible *OsKish* RNAi lines to investigate the influence of OsKish depletion on ER function. Glutelin biogenesis and export from the ER require two functionally distinct classes of factors: molecular chaperones such as PDIL1-1 that facilitate glutelin proper folding and quality control, and COPII-associated factors including GOT1B that mediate cargo export from the ER (Ren et al. 2022). To assess whether OsKish depletion perturbs the spatial organization of these regulatory components, we introduced a GFP-tagged PDIL1-1 reporter into the DEX-inducible *OsKish* RNAi line and analyzed its localization pattern in root tip cells. In addition to its canonical reticular ER localization, PDIL1-1-GFP forms discrete puncta after 6 h of DEX induction (Fig. 4c). Given that GOT1B represents a well-characterized regulator of COPII assembly that localizes specifically to ER exit sites (ERESs; Wang et al. 2016), we generated a GFP-GOT1B transgenic line in the same RNAi background to evaluate ERES integrity. Although GFP-GOT1B retains its punctate pattern irrespective of DEX treatment (Fig. 4d), quantitative analysis revealed that *OsKish* knockdown significantly reduces the size but not the number of GOT1B-positive ERES puncta (Fig. 4e). Collectively, these results indicate that OsKish is indispensable for maintaining both ER proteostasis and the structural integrity of ER export domains.

To further investigate the functional role of OsKish in vegetative tissues, we generated hypomorphic *oskish* alleles using the CRISPR/Cas9-based genome editing system and identified a *cri-oskish* mutant line that phenocopies the endosperm developmental defects, including floury endosperm appearance and impaired glutelin deposition, yet retained the capacity to produce viable roots (Figure S4, a to d). TEM reveals that root cells of the *cri-oskish* mutant accumulate large, electron-dense aggregates composed of disorganized ER tubules, structures that were absent in the WT root cells (Figure S4e). Together with the ER morphology defects observed in *oskish-1* endosperm, these results suggest that OsKish

plays a housekeeping role in maintaining the structural integrity of the tubular ER architecture across rice tissues.

OsKish interacts with the ER shaping regulators OsLNPs and RHD3L.

A recent study in *Arabidopsis* reported that the *lnp1-1 lnp2-1* double mutant exhibits a hyperfused, dense tubular ER network attributable to uncontrolled ER tubule fusion mediated by RHD3 (Sun et al. 2020). This phenotype closely resembles that of the rice *oskish-1* mutant, suggesting a functional relationship among OsKish, LNPs, and RHD3 in the regulation of ER morphology in plants. The rice genome encodes five LNP homologs, designated LNP1–LNP5, and three RHD3-like proteins, designated RHD3L, RHD3L1, and RHD3L2 (Figure S5, a and b). We selected OsLNP1 and OsLNP2 for further study because they harbor domains typically conserved relative to those of Arabidopsis LNP1 and LNP2 (Kriechbaumer et al. 2018). Expression profiling from the Rice Expression Profile Database (http://ricexpro.dna.affrc.go.jp/pro/) reveals that *RHD3L* is the predominantly expressed *RHD3* gene in developing endosperm; accordingly, it was selected for further study.

To delineate the broader interaction network, we systematically investigated potential associations among OsKish, OsLNPs, and RHD3L. Y2H assays confirmed physical interactions between RHD3L and both OsLNP1 and OsLNP2; notably, they also reveal a robust binary interaction between OsKish and RHD3L (Fig. 5a). LCI assays further demonstrated that OsKish interacts with OsLNP1, OsLNP2, and RHD3L in plants, as evidenced by strong luminescence signals specifically detected upon co-expression of each combination (Fig. 5, b to d). These interactions were further verified by Co-IP assays, in which Flag-OsKish could be co-immunoprecipitated by OsLNP1-GFP, OsLNP2-GFP, and GFP-RHD3L but not free GFP from the total protein extracts of *N. benthamiana* (Fig. 5, e to g). BiFC assays localized these interactions predominantly to punctate structures associated with the ER, and critically along continuous tubular ER membranes, specifically for the OsKish–RHD3L combination (Fig. 5h). Collectively, these results indicate that OsKish forms a

cooperative complex crucial for maintaining the structural integrity and dynamic organization of the tubular ER morphology in planta.

OsKish regulates proteasomal degradation of OsLNPs by inhibiting their auto-ubiquitination.

In Arabidopsis, LNP1 and LNP2 function as E3 ubiquitin ligases that target RHD3 for proteasomal degradation, thereby ensuring the structural stability of the tubular ER network (Sun et al. 2020). We next investigated whether OsKish is involved in the ubiquitination of RHD3L by OsLNP1 and OsLNP2 in rice. *In vitro* ubiquitination assays demonstrated that purified OsLNP1-His and OsLNP2-His recombinant proteins each possess intrinsic E3 ligase activity, as evidenced by substantial polyubiquitin chain formation in the presence of ubiquitin (UBQ), E1, and E2 (Fig. 6, a and b). Using the same ubiquitination system, we substantiated that GST-RHD3L is efficiently ubiquitinated by either OsLNP1-His or OsLNP2-His (Fig. 6, b and c). Notably, co-incubation with GST-OsKish altered RHD3L ubiquitination by the OsLNPs (Fig. 6, b and c).

We next investigated whether OsKish modulated RHD3L ubiquitination by disrupting the OsLNPs-RHD3L interaction or suppressing the intrinsic E3 ligase activity of OsLNPs. Given that OsKish, OsLNPs, and RHD3L are integral membrane proteins each containing two transmembrane domains (Chen et al. 2012; Moriya et al. 2013; Sun and Zheng 2018), and considering OsKish's small size and minimal cytosolic domain, we hypothesized that its interaction with RHD3L occurs primarily within transmembrane domains (TMDs). To map the molecular interfaces underlying the OsKish–OsLNP–RHD3L regulatory complex, we generated a series of RHD3L truncation variants, and assessed their interactions in yeast (Figure S6a). Y2H assays revealed that both OsKish and OsLNP1 bind RHD3L predominantly via its TMDs, with a weaker interaction mapped to the C-terminal cytosolic region (Figure S6b). In contrast, LCI assays showed that co-expression of GFP- or mCherry-tagged OsKish did not impair the interaction intensity between OsLNP1 and RHD3L in *N. benthamiana* leaf epidermal cells (Figure S6, c and d), indicating that OsKish does not spatially block this

association in planta. Structural modeling using AlphaFold3 predicted that the OsKish-RHD3L^{TM+CT} complex is stabilized by extensive hydrophobic interactions within the lipid bilayer (Figure S6e).

Given that LNPs and RHD3L are established homooligomers (Bian et al. 2011; Casey et al. 2015; Hu and Rapoport 2016; Wang et al. 2016; Sun and Zheng 2018) and that OsKish undergoes self-interaction (Figure S3, c to e), we employed AlphaFold3 to predict the quaternary structure of a hexamer complex comprising two copies each of OsLNP1, RHD3L, and OsKish. Strikingly, while the OsLNP1–RHD3L binary complex model exhibits conformational flexibility in the N- and C-terminal regions of OsLNP1, incorporation of OsKish induces a marked stabilization of these domains into well-defined, rigid conformations (Figure S6f). Because the N- and C-terminal domains of LNPs harbor the catalytic core essential for E3 ubiquitin ligase activity (Zhao et al. 2016; Sun et al. 2020), this structural transition suggests that OsKish modulates OsLNP1's enzymatic function by enforcing a catalytically restrained conformation. Comparative interface analysis using PyMOL further reveals substantial remodeling of the OsLNP1–RHD3L interaction surface upon OsKish binding, including shifts in key interfacial residues and altered contact topology, despite preservation of overall binding affinity (Fig. S6g). Collectively, these computational insights provide a predictive framework for the experimental observation that OsKish alters RHD3L ubiquitination without disrupting the physical association between OsLNP1 and RHD3L.

Using the same reconstituted *in vitro* ubiquitination system, we found that OsKish suppresses the auto-ubiquitination of both OsLNP1-His and OsLNP2-His (Fig. 6g). To extend these findings to a physiological context, we performed an *in vitro* ubiquitination assay (Lin et al., 2012) using total protein extracts from DEX-inducible *OsKish* RNAi plants with or without DEX treatment to assess OsLNP auto-ubiquitination. Consistently, *OsKish* knockdown led to a substantial increase in polyubiquitin conjugates associated with both OsLNP1 and OsLNP2 (Fig. 6g). Immunoblotting with linkage-specific ubiquitin antibodies anti-K48 and anti-K63 confirmed that the predominant modification of OsLNPs is K48-linked, rather than K63-linked, polyubiquitination (Fig. 6g). Given that K48-linked chains

typically target substrates for 26S proteasomal degradation, we hypothesized that OsKish-mediated suppression of OsLNP auto-ubiquitination stabilizes these E3 ligases *in vivo*. To test this, we first assessed the *in vivo* ubiquitination of RHD3L in *DEX::OsKish-RNAi*/GFP-RHD3L lines and found that OsKish depletion resulted in reduced ubiquitination levels of RHD3L (Fig. 6h). We then employed a cell-free protein degradation assay (Sun et al. 2021) using cytosolic extracts from the same DEX-inducible lines. As predicted, both OsLNP1 and OsLNP2 exhibited accelerated degradation kinetics upon OsKish depletion, whereas RHD3L exhibited slower degradation (Fig. 6i). Collectively, these results demonstrate that OsKish functions as a critical negative regulator of OsLNP auto-ubiquitination, thereby preserving OsLNP protein stability and sustaining their E3 ligase activity in rice.

Over-accumulation of RHD3L in both *oskish-1* and *oslnp1-1 oslnp2-1* mutants.

To test whether OsLNP1 and OsLNP2 play a conserved role in regulating ER morphology, as in Arabidopsis, we generated the *oslnp1* and *oslnp2* single mutants using the CRISPR/Cas9 system and produced the *oslnp1-1 oslnp2-1* double mutant by crossing (Figure S5, c and d). As expected, the *oslnp1-1 oslnp2-1* double mutant but not either of the single mutants exhibit phenotypic defects similar to those of *oskish-1* in endosperm appearance, root growth, glutelin deposition, and ER morphology (Fig. 7, a to e), indicating that the function of LNP proteins in regulating ER morphology is evolutionarily conserved across plants.

We next raised anti-RHD3L polyclonal antibodies to examine whether the *OsKish* mutation influences the accumulation of the RHD3L protein in rice. The RHD3L antibodies recognized an ~100 kDa band in total protein extracts from WT endosperm and a relatively faint band of the same size in the *RHD3L* knockout mutant (Figure S7a). The faint band observed in the *cri-rhd3l-2* mutant may correspond to other RHD3L homologs. Alternatively, it may represent a truncated RHD3L protein resulting from premature termination, which is predicted to lack 17 amino acid residues (Figure S5e), yet this region is reported to be essential for efficient ER fusion (Sun and Zheng 2018). Immunoblotting using anti-RHD3L antibodies, combined with quantification, showed that RHD3L is over-accumulated in the

oskish-1 mutant and the *oslnp1-1 oslnp2-1* double mutant (Figure S7, b to f). Additionally, RT-qPCR analysis showed that the transcription level of *RHD3L* was dramatically upregulated in *DEX::OsKish-RNAi* plants after DEX induction (Figure S7f), implying a possible feedback regulation mechanism resulting from the OsKish depletion. These results indicate that the *OsKish* mutation increases the abundance of RHD3L protein, thereby leading to excessive ER membrane fusion in rice.

Moreover, we generated transgenic plants expressing GFP-tagged OsLNP1 and RHD3L in DEX-inducible *OsKish* RNAi plants and examined their subcellular localization patterns in root tip cells. In the absence of DEX induction, OsLNP1-GFP localized to both punctate and reticular structures, while GFP-RHD3L displayed a clear reticular pattern (Figure S8, a and b). After 6 h dark treatment with DEX induction, the punctate signals of OsLNP1-GFP disappeared (Figure S8a). Interestingly, GFP-RHD3L formed punctate fluorescent foci of varying sizes (Figure S8b). Statistical analysis revealed that the large GFP-RHD3L fluorescent puncta observed by confocal microscopy closely correspond in size to the electron-dense ER aggregates identified by TEM in root tip cells of the *cri-oskish* mutant. The strong correlation observed between the physical dimensions of the structures resolved by the two imaging methods suggests that RHD3L is enriched in ER aggregates (Figure S8c).

OsKish suppresses the fusion activity of RHD3L possibly by influencing its oligomerization

To uncover the biological significance of the physical interaction between OsKish and RHD3L, we first investigated the functional conservation of RHD3L in maintaining the ER structure in rice. Confocal microscopy revealed that the ER exhibited a typical reticular network when mRFP-HDEL was expressed alone in *N. benthamiana* leaf cells (Fig. 8a). However, upon co-expression with GFP-RHD3L, the ER structure showed an increase in sheet-like ER (Fig. 8b). We defined a sheet as a relatively expanded, flattened ER region occupied by several three-way junctions (Sun et al. 2020). This observation suggests that RHD3L, similar to its Arabidopsis counterpart, promotes homotypic ER fusion. When

OsLNP1-mCherry or OsLNP2-mCherry was co-expressed with GFP-RHD3L, the network structure reappeared (Fig. 8, c and d). Interestingly, co-expression of mCherry-OsKish with GFP-RHD3L also reduced the RHD3L-induced sheet-like ER structures and restored a clear reticular ER; both OsKish and RHD3L colocalized in the reticular ER and at its three-way junctions (Fig. 8e). ImageJ-based quantification revealed that the average percentage of ER sheets in cells expressing mRFP-HDEL alone was approximately 5%. When GFP-RHD3L was co-expressed, the percentage increased dramatically to 25%. More interestingly, when OsKish was co-expressed with RHD3L, it decreased to approximately 6% (Fig. 8f). These results suggest that OsKish inhibits the excessive fusion by RHD3L, thereby maintaining normal ER structure in planta.

Cumulative evidence from Arabidopsis suggests that RHD3 oligomerization is required for RHD3-mediated efficient ER membrane fusion (Zheng and Chen 2011; Sun and Zheng 2018). *In vitro* pull-down assays confirmed the self-interaction of RHD3L, whereas OsKish inhibits this self-interaction (Fig. 9a). LCI assays verified RHD3L self-interaction and showed that co-expression of GFP- or mCherry-tagged OsKish substantially diminished RHD3L self-interaction in *N. benthamiana* leaf epidermal cells (Fig. 9, b and c). Furthermore, BiFC assays showed that RHD3L interacts with itself predominantly at the ER three-way junctions, and also on ER tubules, in *N. benthamiana* leaf epidermal cells (Fig. 9, d to g). Interestingly, upon co-expression with OsKish, the fluorescence signals were substantially reduced, as evidenced by quantification of fluorescence intensity (Fig. 9h). Immunoblotting confirmed comparable abundance of RHD3L with or without *OsKish* expression in the transient expression system (Fig. 9i). Taken together, these results suggest that OsKish maintains the tubular ER structure possibly by modulating RHD3L oligomerization in rice.

To determine the genetic relationship between *RHD3L* and *OsKish*, we generated *RHD3L* knockout lines in both the WT and *oskish-1* backgrounds. *RHD3L* knockout in the WT background caused no visible endosperm appearance phenotype, whereas *RHD3L* knockout in the *oskish-1* mutant partially rescued the endosperm appearance of *oskish-1* (Fig. S9a). Immunoblotting with anti-RHD3L antibodies confirmed the effectiveness of the *RHD3L* knockout (Figure S9, b and c). Furthermore, TEM reveals canonical PBs but short,

segmented ER tubules in the *cri-rhd3l* line compared with the WT (Figure S9d). In the *RHD3L* knockout lines in the *oskish-1* background, the dense ER tubule aggregates are almost absent, yet round protein particles of distinct size remained in the ER (Figure S9, d and e). Taken together, these results indicate that *OsKish* and *RHD3L* coordinately regulate ER tubule morphology.

Discussion

In this study, through map-based cloning and functional characterization of the *gpa15* mutant, we identified OsKish as a key regulator of ER morphology that ensures proper ER tubule fusion in rice, based on several lines of evidence: (1) TEM analysis of developing endosperm and root tip cells reveals severe defects in ER morphology due to excessive fusion of ER tubules in the *oskish-1* mutant; (2) OsKish interacts with OsLNPs, and depletion of OsLNPs caused a similar ER phenotypic defect, suggesting that OsKish and OsLNPs function in a common genetic pathway; (3) OsKish suppresses the auto-ubiquitination activity of OsLNPs, thereby regulating the stability of three-way junctions ; (4) OsKish is required for the proper localization of OsLNP1 , and its deletion leads to over-accumulation of RHD3L; (5) OsKish interacts with RHD3L and inhibits ER membrane fusion possibly by disrupting its oligomerization; and (6) Knockout of *RHD3L* in the *oskish-1* mutant substantially diminished the dense ER tubule aggregates. Collectively, our findings support the proposed working model that OsKish functions together with LNPs and RHD3-like proteins to fine-tune ER membrane fusion in plants.

Cumulating evidence substantiates that stabilization of three-way junctions by LNPs is essential for the maintenance and dynamic remodeling of the tubular ER network (Shemesh et al. 2014; Chen et al. 2015; Wang et al. 2016). AlphaFold3-predicted structural models of the OsKish–RHD3L, OsLNP1–RHD3L, and OsKish–OsLNP1–RHD3L complexes suggest that OsKish binding induces conformational rigidity in the OsLNP1 termini, shifting them from a flexible to a structurally ordered state (Figure S6). This prediction offers a mechanistic hypothesis that OsKish may modulate OsLNP1 's E3 ubiquitin ligase activity. However, high-

resolution structural validation such as cryo-EM or X-ray crystallography remains essential. Our results demonstrate that OsKish functions as a positive regulator of OsLNPs through modulating their auto-ubiquitination (Figure 6). The ubiquitination assays confirmed that OsKish suppresses OsLNPs auto-ubiquitination both *in vivo* and *in vitro*, thereby maintaining their stability. Notably, RHD3L ubiquitination levels differ between *in vivo* and *in vitro* assays; this discrepancy most likely arises from differential stability of the E3 ligases. *In vivo*, OsKish depletion induces auto-ubiquitination and subsequent proteasomal degradation of OsLNPs, resulting in substantially reduced protein abundance. Consequently, diminished OsLNPs' protein levels attenuate RHD3L ubiquitination and delay its turnover, thereby obscuring the direct enzymatic activity of OsLNPs observed under reconstituted *in vitro* conditions.

Previous studies in *Arabidopsis* reported that RTNLB3 inhibits the fusion activity of RHD3, partly by disrupting RHD3 oligomerization (Wang and Zheng 2024). The interaction between RTNL13 and RHD3 also occurs at specific sites along ER tubules and at certain three-way junctions (Wang and Zheng 2024). ER tubule-forming proteins are evolutionarily conserved, and a common feature of all these proteins is the reticulon homology domain (RHD), which consists of two consecutive transmembrane (TM) hairpin domains (Shibata et al. 2008; Sparkes et al. 2010; Tolley et al. 2010). Consistently, we found that *OsKish* expression substantially inhibits the RHD3L oligomerization (Figure 9), a process essential for its membrane fusion activity. Together, the ubiquitination- and oligomerization-mediated regulatory layers appear to act synergistically to ensure precise spatiotemporal control of ER membrane fusion in plants. Nevertheless, the exact causal relationships underlying this coordination require further experimental validation in future studies.

ERESs are specialized ER membrane domains that drive coat protein complex II (COPII) assembly and thus play crucial roles in the ER export of secretory proteins in eukaryotes (Budnik and Stephens 2009). ERES formation and functionality greatly depend on regions of high membrane curvature, particularly the edges of ER tubules and sheet boundaries (Okamoto et al. 2012). Our previous studies reported that GOT1B mediates COPII assembly at ERESs in rice, and its depletion causes ER retention of glutelins in rice endosperm cells

(Wang et al. 2016). In this study, we demonstrate that OsKish depletion impairs glutelin export from the ER, coinciding with aberrant ER hyper-fusion mediated by increased RHD3L protein abundance (Fig. 2; Figure S7b). In addition, in the *OsKish* RNAi line, GFP-GOT1B fluorescence puncta were significantly smaller upon *OsKish* knockdown, implying defective COPII assembly and consequent impairment of glutelin export (Figure 4). RHD3 has been shown to be required for normal ER structure and anterograde membrane trafficking, facilitating transport of secretory cargo and Golgi-resident proteins between the ER and Golgi apparatus (Zheng et al. 2004). Notably, knockdown of *RHD3L* in the *oskish-1* mutant partially restored the ER tubule morphology defect but failed to rescue glutelin export. This phenotypic dissociation suggests that the glutelin ER retention phenotype in *oskish-1* arises from mechanisms independent of RHD3L-mediated membrane fusion. The persistence of the glutelin export defect implies that OsKish likely possesses additional functions beyond regulating ER homeostasis, or that parallel RHD3L-independent pathways contribute to COPII-dependent ER export. Future studies should aim to elucidate these potential RHD3L-independent mechanisms and the intrinsic molecular relationship between ER homeostasis and protein export in plants.

Methods

Plant materials and growth conditions

Two allelic *gpa15* mutants, *gpa15-1* and *gpa15-2*, were isolated in this study. *gpa15-1* was derived from an EMS-treated M_2 population of the *japonica* rice cultivar Kitaake, and *gpa15-2* was isolated from an MNU-treated M_2 population of the *japonica* rice cultivar Ningjing 1. As the *gpa15* ($^{-/-}$) homozygous mutant is seedling lethal, the *gpa15* mutation was maintained in the heterozygous form. To remove background mutations, the heterozygous *gpa15* mutants were backcrossed to their corresponding wild-type cultivars at least three times. The *gpa15* ($^{-/-}$) homozygous hulled seeds were surface sterilized and grown in culture boxes containing 1/2 Murashige and Skoog (MS) medium supplemented with 0.7% agar and 1%

sucrose at 28°C. Unless indicated otherwise, rice plants were grown in paddy fields during normal growing seasons or in a greenhouse.

Antibodies

Anti-glutelin acidic subunits, anti-glutelin basic subunits, anti-α-globulin, anti-prolamin, anti-BiP1, and anti-PDIL1-1 were described previously (Wang et al. 2016; Ren et al. 2020). Anti-GFP (dilution 1:3000; 11814460001, Roche), anti-Flag (dilution 1:3000; F1804, Sigma-Aldrich), anti-EF-1α (dilution 1:3000; AS10 934, Agrisera), anti-GST (dilution 1:3000; PM013-7, MBL), anti-His (dilution 1:3000; D291-7, MBL), anti-UBQ (dilution 1:1000; P4D1; Cell Signaling Technology) , anti-K48 (dilution 1:1000; 05-1307, Millipore), and anti-K63 (dilution 1:1000; 05-1308, Millipore) antibodies are commercially available. Partial coding sequence (CDS) of RHD3L (Os01g0575000, amino acid residues 722–806) was cloned into the pET-28a-SUMO vector, and the expressed recombinant protein was injected into rabbits to generate polyclonal antibodies at ABclonal Biotechnology.

Protein extraction-related assays, SDS-PAGE, and immunoblotting

Total seed protein extraction and SDS-PAGE analysis were performed as previously described (Wang et al. 2016; Ren et al. 2020). Briefly, hulled rice seeds were ground into flour, and then suspended in a lysis buffer containing 4% (w/v) SDS, 4 M urea, 5% (v/v) β-mercaptoethanol, and 125 mM Tris-HCl at pH 6.8.

For protein extraction from plants, 10-day-old plant seedlings or *N. benthamiana* leaves were ground to powder in liquid nitrogen. The samples were then resuspended in ice-cold NB1 buffer (50 mM Tris-MES (pH 8.0), 1 mM $MgCl_2$, 0.5 M Sucrose, 10 mM EDTA (pH 8.0), 5 mM DTT, 0.1% (v/v) Nonidet P-40, 1×Complete Protease Inhibitor Cocktail). After incubation at 4°C for 20 min, the homogenates were centrifuged at 2,000*g* for 10 min at 4°C and filtered through cheesecloth to remove cell debris; the filtrate was then centrifuged at 10,000*g* for 10 min at 4°C for subsequent analyses.

SDS-PAGE analysis was performed on a 12.5% (v/v) uniform gel, followed by CBB staining or immunoblotting. Antibody-antigen reactions were detected with the ECL detection reagent (Thermo Scientific) and visualized with the ECL detection system (LI-COR, Odyssey-Fc).

All immunoblot analyses were independently repeated with at least three biological replicates (three independent seeds, seedlings, or *N. benthamiana* leaves, as required for different experiments), yielding consistent results; representative results are presented. Quantification of immunoblotting data was performed using ImageJ software (https://imagej.nih.gov/ij/) as previously described (Ren et al. 2020).

Microscopy observation

Scanning electron microscopy, immunofluorescence analysis, transmission electron microscopy, and subsequent immunogold labeling experiments were performed as previously described (Wang et al. 2010; Liu et al. 2013; Ren et al. 2020) with minor modifications. Briefly, for scanning electron microscopy, transverse sections of the wild-type and *gpa15* dry seeds were sputter-coated with gold palladium and then observed using a scanning electron microscope (Hitachi S-3400N, Tokyo, Japan).

For immunofluorescence analysis, 0.4 μm-thick semithin sections of developing endosperm were blocked in Tris-buffered saline with Tween 20 (TBST) containing 3% (w/v) BSA for 1 h and then incubated with combinations of primary antibodies diluted in blocking buffer containing 1% (w/v) BSA, followed by three washes with TBST. Sections were then incubated with Alexa Fluor 488 (green)- and Alexa Fluor 555 (red)-conjugated secondary antibodies (Invitrogen), washed three times with TBST, and observed using a Zeiss LSM980 laser scanning confocal microscope. Sections were incubated with primary antibodies against glutelin acidic subunits (dilution 1:5000), 13 kDa prolamin (dilution 1:5000), and secondary antibodies (dilution 1:5000).

For transmission electron microscopy, ~1 mm-thick transverse sections of developing endosperm from wild-type and *gpa15* plants were fixed in 2.5% glutaraldehyde and 0.5% paraformaldehyde buffered with 0.2 M phosphate buffer (pH 7.2) for more than 12 h, followed by three washes with ultrapure water or phosphate buffer. The samples were then post-fixed using a 1–2% OsO_4 for 2–3 h until the endosperm periphery turned black. For dehydration, a graded acetone series was employed: samples were sequentially incubated in 50%, 70%, 80%, and 90% acetone for 20 min each, followed by six changes of 100% acetone. Infiltration was performed using a gradient mixture of acetone and resin: initially with a 3:1 (acetone: resin) ratio for 30 min, followed by a 1:1 ratio for 4 h, and finally a 1:3 ratio overnight in a 30°C oven to volatilize acetone. After infiltration, the sample was transferred into embedding molds filled with fresh embedding medium and incubated in a 30°C oven for ~7 h. The blocks were then polymerized sequentially at 37°C, 45°C, and 60°C for 48 h each to complete resin curing. Ultrathin sections (70 nm thick) were prepared with a Leica EM UC7 microtome and examined with a Hitachi H7700 transmission electron microscope.

For immunogold electron microscopy, ~1 mm-thick transverse sections of developing endosperm from wild-type and *gpa15* plants were fixed in 2.5% glutaraldehyde and 0.5% paraformaldehyde buffered with 0.2 M phosphate buffer (pH 7.2) for more than 12 h, followed by a graded series of ethanol dehydration. The samples were then embedded in LOWICRYL HM20 resin via UV light polymerization (AFS2, Leica). Ultrathin sections (70 nm thick) were prepared using a Leica EM UC7 microtome. Immunogold labeling was performed with primary antibodies at 50 μg/mL and 10- or 15-nm gold-conjugated secondary antibodies diluted at 1:50 (Abcam). After post-staining with aqueous uranyl acetate and lead citrate, the samples were examined using a Hitachi H7700 transmission electron microscope.

Map-based cloning

To map the *GPA15* locus, the *gpa15* ($^{+/-}$) heterozygous plant was crossed with the *indica* variety Dular to produce a mapping population. F_2 seeds were individually harvested from

the F_1 plants. F_2 grains exhibiting the *gpa15*-like phenotype were selected to map the *gpa15* locus using the half-grain method (Ren et al. 2020). To perform phenotyping and mapping simultaneously, F_2 grains with floury endosperm were cut into two halves. The embryoless half was ground into flour and analyzed by SDS-PAGE to assess storage protein accumulation phenotype. Meanwhile, the half containing the embryo defective in glutelin precursor accumulation was subjected to DNA extraction for mapping. A total of 292 recessive individuals were used for fine mapping of *GPA15*. Primers used in fine mapping are listed in Supplemental Data Set 1.

Phylogenetic analysis

Putative homologs of OsKish in eukaryotes were identified using the BLASTP program at the National Center for Biotechnology Information (http://www.ncbi.nlm.nih.gov). The phylogenetic tree was constructed using MEGA 11 (http://www.megasoftware.net) based on the neighbor-joining method with the following parameters: p-distance model, pairwise deletion, and bootstrap (1000 replicates; random seed). The multiple sequence alignment used to generate this phylogeny is provided as a FASTA file labeled Supplemental File 1 and a Newick (.nwk) file labeled Supplemental File 2.

Y2H assay

Y2H assays were used to detect protein interactions using the DUAL HUNTER system (Dualsystems Biotech). The indicated sequences were fused to the Cub fragment in the pXGY17 vector or to the Nub fragment in the pXGY18 vector. Y2H assays were conducted according to the method described previously (Wang et al. 2021). Corresponding plasmids were co-transformed into the yeast strain NMY51 following the manufacturer's instructions. Primers used in this assay are listed in Supplemental Data Set 1.

RT-qPCR analysis

Total RNA was isolated using the RNAprep Pure Plant Kit (Tiangen). The first-strand cDNA was synthesized using PrimeScript Reverse Transcriptase (Takara) for reverse transcription. Rice *Ubiquitin* (*UBQ*) was used as an internal control. Real-time PCR analysis was performed using an ABI 7500 real-time PCR system with SYBR Green Mix (Bio-Rad) and three biological repeats (three independent plants). The relative expression levels of target genes were determined using the delta-delta Ct method ($2^{-\Delta\Delta Ct}$; Livak and Schmittgen 2001). Briefly, the Ct values of the target genes were first normalized to the internal control gene (ENDO) to obtain the Δ*Ct* value ($\Delta Ct = C_{t,\ Target} - C_{t,\ ENDO}$). The Δ*Ct* values were then calibrated against the treated/experimental sample to obtain the ΔΔ*Ct* value. The relative expression (fold change) was calculated as 2^-(ΔΔ*Ct*). Primers used in this assay are listed in Supplemental Data Set 1.

Vector construction and rice transformation

For the complementation test, a 6,394-bp wild-type genomic fragment spanning the regulatory elements, including a 1,998-bp promoter and a 1,049-bp downstream regulatory region, was cloned into the pCAMBIA2300 vector to generate the pGPA15::GPA15 construct. The GFP/mCherry/Flag fusion constructs used for transient expression in *N. benthamiana* leaf epidermal cells were created by cloning PCR-amplified CDS into the pCAMBIA1305 backbone containing the CaMV 35S promoter. The construct driven by the dexamethasone (DEX) promoter-inducible was generated as previously described (Huang et al. 2022). Briefly, a 213-bp fragment of *GPA15* was amplified as two overlapping fragments and inserted into the hairpin RNAi vector TBI001. The *GPA15* RNAi fragment was cloned downstream of the DEX-inducible promoter from pTA7002. To generate weak alleles of *OsKish* via CRISPR/Cas9-mediated genome editing, we used saturated targeted endogenous mutagenesis editors (STEMEs), which enable *de novo* mutation generation and facilitate directed evolution of plant genes (Li et al. 2020). PH-STEME7, PH-STEME7-NG, and PH-STEME7-SpRY were used with 20 individual single-guide RNAs (sgRNAs), each incorporating Cas9-NGG, Cas9-NG,

and Cas9-NNN protospacer-adjacent motif (PAM) variants, respectively. Target fragments were ligated into the vector. The resulting constructs were transformed into the japonica cultivar Nipponbare, and transgenic lines were genotyped by PCR and Sanger sequencing. To generate the *OsLNPs* and *RHD3L* knockout mutants via CRISPR-Cas9, sgRNAs targeting each gene were designed using CRISPR-P (http://cbi.hzau.edu.cn/cgi-bin/CRISPR). Target fragments were ligated into the sgRNA-Cas9 vector. The resulting constructs were transformed into *gpa15-1* or Kitaake, and transgenic lines were genotyped by PCR and Sanger sequencing. Primers used to generate the corresponding constructs are listed in Supplemental Data Set 1. All constructs were confirmed by restriction digestion and DNA sequencing.

LCI assay

For the interaction assay between OsKish and itself, the CDS of *OsKish* was fused upstream of NLUC in the pCAMBIA-NLUC vector and the downstream of CLUC in the pCAMBIA-CLUC vector. For the interaction assay between RHD3L and itself, the CDS of *RHD3L* was fused upstream of NLUC in the pCAMBIA-NLUC vector and downstream of CLUC in the pCAMBIA-CLUC vector. These constructs were transformed into the EHA105 strain, and various combinations of EHA105 strains were infiltrated into *N. benthamiana* leaves. After 24 to 48 h, the relative LUC activity was measured. Each combination was tested with at least three replicates (three independent experiments).

BiFC assay

The CDSs of *OsKish* and *RHD3L* were cloned into p2YN and p2YC vectors to generate the Y^N-OsKish and Y^N-RHD3L as well as Y^C-RHD3L and Y^C-OsKish constructs, respectively. These constructs were then transformed into the EHA105 strain, and various combinations of EHA105 strains were infiltrated into *N. benthamiana* leaves. After 24 to 48 h, protoplasts

were isolated from the infiltrated leaves, and fluorescence signals were captured using a Zeiss LSM980 laser scanning confocal microscope.

Co-IP assay

The CDSs of *OsKish* or *RHD3L* were separately cloned into the pCAMBIA1305-GFP and pCAMBIA1300-221-Flag vectors (Ren et al. 2014) to generate GFP-OsKish, Flag-OsKish, and GFP-RHD3L constructs. These constructs were transformed into the EHA105 strain and infiltrated into *N. benthamiana* leaves. After 24 to 48 h, total leaf protein lysates were prepared in ice-cold IP buffer (50 mM Tris-MES pH 7.5, 1 mM $MgCl_2$, 0.5 M sucrose, 10 mM EDTA, 5 mM DTT, 0.1% [v/v] Nonidet P-40, and 1× Complete Protease Inhibitor Cocktail) and were incubated with GFP-Trap magnetic beads (ChromoTek) for 2 h at 4°C with rotation. After washing three times with IP buffer, the immunoprecipitated samples were eluted in reducing buffer, followed by SDS-PAGE and immunoblotting analyses using anti-GFP (dilution 1:3000) and anti-Flag (dilution 1:3000) antibodies.

***In vitro* ubiquitination assay**

In vitro ubiquitination assays were performed as described previously (Wang et al. 2024). Recombinant GST-RHD3L, GST-GPA15, OsLNP1-His, OsLNP1-His, E1 (His-AtUBA2), and E2 (His-AtUBC10) were purified using BeaverBeads™ GSH (70601-100, Beaver) and IDA-Nickel (70501-K100, Beaver), respectively. A total of 50 ng E1, 100 ng E2, 2 μg Flag-Ub (BostonBiochem, U120), 2 μg GST-RHD3L, and 2 μg OsLNP1-His or OsLNP2-His were incubated in ubiquitination reaction buffer (50 mM Tris-HCl pH 7.5, 10 mM $MgCl_2$, 5 mM ATP, and 2 mM dithiothreitol) at 30°C for 1 h. After the reaction, samples were mixed with 5× protein loading buffer and boiled for 5 min at 95°C, which were subjected to immunoblotting with anti-GST and anti-His antibodies (dilution 1:5000). Polyubiquitination of RHD3L was detected with anti-Ub (dilution 1:1000) antibody.

Another type of *in vitro* ubiquitination assay was conducted using total protein extracts, as described previously (Lin et al. 2012) with some modifications. Purified OsLNP1-His bound to IDA-Nickel beads (70501-K100, BEAVER) was incubated at 28°C with equal amounts of rice seedling crude extract in a buffer containing 25 mM Tris-HCl pH 7.5, 10 mM $MgCl_2$, 10 mM NaCl, 0.5% [v/v] Nonidet P-40, 10 mM ATP, 4% [v/v] 50× Protease Cocktail, and 40 μM MG132. After incubation at 28°C for 20–30 min, samples were mixed with 5× protein loading buffer and boiled for 5 min at 95°C, then subjected to immunoblotting with anti-His (dilution 1:5000), anti-UBQ (dilution 1:1000), anti-K48-linked ubiquitin chain (Millipore, 05-1307), or anti-K63-linked ubiquitin chain polyclonal (Millipore, 05-1308) antibodies.

Semi-*in vitro* cell-free protein degradation assay

Semi–*in vitro* cell-free protein degradation assays were performed as previously described (Sun et al. 2020). Total protein was extracted using degradation buffer (50 mM Tris-HCl, pH 7.5, 150 mM NaCl, 10 mM $MgCl_2$, 0.5% [v/v] Nonidet P-40, 4 μM phenylmethylsulfonyl fluoride [PMSF] and 10 mM ATP). After incubation at 28°C for the intervals as indicated, samples were added with 5× protein loading buffer and boiled at 95°C for 5 min. The samples were loaded onto 10% (w/v) SDS-PAGE gels for immunoblotting with anti-His antibody (dilution 1:5000).

Quantification and statistical analysis

Quantifications were performed using ImageJ. Statistical analysis methods are specified in the figure legends. Student's *t*-test, one-way ANOVA were conducted using GraphPad Prism 8 (version 8.0.2). The sample size (*n*), statistical tests used, and exact *P* values are indicated in the corresponding figure legends. Differences were considered statistically significant at $P < 0.05$. The analyzed results are listed in Supplemental Data Set 2.

Accession numbers

Sequence data from this study can be found in the GenBank/EMBL libraries under the following accession numbers: *OsKish/GPA15* (*Os05g0251500*), *OsKish-L* (*Os02g0299600*), *RHD3L* (*Os01g0575000*), *RHD3L-1* (*Os12g0604600*), *RHD3L-2* (*Os11g0582300*), *OsLNP1* (*Os04g0672900*), and *OsLNP2* (*Os02g0631000*). The accession numbers for proteins in the phylogenetic analysis are as follows: NcKish, XP_031490721.1; ObKish, XP_015689023.1; ObKish-A, XP_015692421.1; MtKish, XP_003601807.1; SbKish-1, NP_001352018.1; SbKish-2, XP_021303185.1; ZmKish, NP_001352018.1; HvKish, XP_044966093.1; DmKish, NP_652499.2; AcKish, XP_020087835.1; VvKish, XR_009464450.1; SlKish-1, XP_010318675.1; SlKish-2, XP_004241667.1; NnKish-1, XP_010266584.1; NnKish-2, XP_010267560.1; AtKish, NP_001078607.1; MmKish-A-1, XP_001111642.1; MmKish-A-2, XP_036009505.1; OaKish, XP_004009113.1; SsKish, XP_058492184.1; NtKish-1, XP_016485151.1; NtKish-2, XP_016471715.1; NtKish-3, XP_016487752.1; HKish-A, NP_777569.1; XlKishA, NP_001165257.1; SmKish-1, XP_024532558.1; SmKish-2, XP_024538342.1.

Acknowledgments

We thank the Core Facility Platform, Institute of Crop Sciences, Chinese Academy of Agricultural Sciences, for their assistance with confocal imaging and transmission electron microscopy analysis. We thank Zhongshan Biological Breeding Laboratory, Jiangsu Nanjing Rice Germplasm Resources National Field Observation and Research Station for careful field management.

Author Contributions

J.W. and Y.R. conceived and supervised the project. P.Z., Y.W., and Y.R. designed the experiments. P.Z. performed most of the experiments. Y.Z., Yu Z., X.H., Y.C., J.Z., B.L., X.B., H.W., F.W., X.W., A.Z., C.L., Y.L., C.L.L., and Z.C. participated in the experiments. Y.R., P.Z.,

H.W., and Y.W. analyzed the data and wrote the paper. All authors contributed substantially to this study, read, and approved the final version of the manuscript.

Funding

This work was supported by grants from the National Key Research and Development Program of China (2021YFF1000200), the National Natural Science Foundation of China (31830064 and 32172085), the Basic Research Center of Innovation Program of Chinese Academy of Agricultural Sciences (CAAS-CSNCB-202302), the Central Public-interest Scientific Institution Basal Research Fund (Y2025YC02), the Fundamental Research Funds for the Central Universities (KYZZ2025008), and the Inner Mongolia Innovation Center of Biological Breeding Technology (2025-2027). This work was also supported by the earmarked fund for China Agriculture Research System (CARS-01-05).

References

Anwar K et al. 2012. The dynamin-like GTPase Sey1p mediates homotypic ER fusion in *S. cerevisiae*. J Cell Biol. 197:209–217. https://doi.org/10.1083/jcb.201111115.

Bao X et al. 2023. A deleterious Sar1c variant in rice inhibits export of seed storage proteins from the endoplasmic reticulum. Plant Mol Biol. 111:291–307. https://doi.org/10.1007/s11103-022-01327-z.

Baumann O, Walz B. 2001. Endoplasmic reticulum of animal cells and its organization into structural and functional domains. Int Rev Cytol. 205:149–214. https://doi.org/10.1016/S0074-7696(01)05004-5.

Bian X et al. 2001. Structures of the atlastin GTPase provide insight into homotypic fusion of endoplasmic reticulum membranes. Proc Natl Acad Sci U S A. 108:3976–3981. https://doi.org/10.1073/pnas.1101643108.

Bottanelli F, Gershlick DC, Denecke J. 2012. Evidence for sequential action of RAB5 and RAB7 GTPases in prevacuolar organelle partitioning. Traffic. 13:338–354. https://doi.org/10.1111/j.1600-0854.2011.01303.x.

Brandizzi F. 2021. Maintaining the structural and functional homeostasis of the plant endoplasmic reticulum. Dev Cell. 56:919–932. https://doi.org/10.1016/j.devcel.2021.02.008.

Budnik A and Stephens DJ. 2009. ER exit sites – Localization and control of COPII vesicle formation. FEBS Letters. 583:3796–3803. https://doi.org/10.1016/j.febslet.2009.10.038.

Casey AK, Chen S, Novick P, Ferro-Novick S, Wente SR. 2015. Nuclear pore complex integrity requires Lnp1, a regulator of cortical endoplasmic reticulum. Mol Biol Cell. 26:2833–2844. https://doi.org/10.1091/mbc.E15-01-0053.

Chen J, Doyle C, Qi X, Zheng H. 2012a. The endoplasmic reticulum: a social network in plant cells. J Integr Plant Biol. 54**:**840–850. https://doi.org/10.1111/j.1744-7909.2012.01176.x.

Chen J, Stefano G, Brandizzi F, Zheng H. 2011. *Arabidopsis* RHD3 mediates the generation of the tubular ER network and is required for Golgi distribution and motility in plant cells. J Cell Sci. 124:2241–2252. https://doi.org/10.1242/jcs.084624.

Chen S et al. 2015. Lunapark stabilizes nascent three-way junctions in the endoplasmic reticulum. Proc Natl Acad Sci U S A. 112:418–423. https://doi.org/10.1073/pnas.1423026112.

Chen S, Novick P, Ferro-Novick S. 2012b. ER network formation requires a balance of the dynamin-like GTPase Sey1p and the Lunapark family member Lnp1p. Nat Cell Biol. 14:707–716. https://doi.org/10.1038/ncb2523.

Fagone P, Jackowski S. 2009. Membrane phospholipid synthesis and endoplasmic reticulum function. Nat Cell Biol. 50:S311–S316. https://doi.org/10.1194/jlr.R800049-JLR200.

Friedman JR, Voeltz GK. 2011. The ER in 3D: a multifunctional dynamic membrane network. Trends Cell Biol. 21:709–717. https://doi.org/10.1016/j.tcb.2011.07.004.

Gao C et al. 2014. A unique plant ESCRT component, FREE1, regulates multivesicular body protein sorting and plant growth. Curr Biol. 24:2556–2563. https://doi.org/10.1016/j.cub.2014.09.014

Hu J, Prinz WA, Rapoport TA. 2011. Weaving the web of ER tubules. Cell. 147:1226–1231. https://doi.org/10.1016/j.cell.2011.11.022.

Hu J, Rapoport TA. 2016. Fusion of the endoplasmic reticulum by membrane-bound GTPases. Semin Cell Dev Biol. 60:105–111. https://doi.org/10.1016/j.semcdb.2016.06.001.

Huang S et al. 2022. The plant ESCRT component FREE1 regulates peroxisome-mediated turnover of lipid droplets in germinating *Arabidopsis* seedlings. Plant Cell. 34:4255–4273. https://doi.org/10.1093/plcell/koac195.

Jang E et al. 2023. Yeast lunapark regulates the formation of *trans*-Sey1p complexes for homotypic ER membrane fusion. iScience. 26:108386. https://doi.org/10.1016/j.isci.2023.108386.

Kriechbaumer V et al. 2018. *Arabidopsis* Lunapark proteins are involved in ER cisternae formation. New Phytol. 219:990–1004. https://doi.org/10.1111/nph.15228.

Li C et al. 2020. Targeted, random mutagenesis of plant genes with dual cytosine and adenine base editors. Nat Biotechnol. 38:875–882. https://doi.org/10.1038/s41587-019-0393-7.

Lin Q et al. 2012. Rice APC/CTE controls tillering by mediating the degradation of MONOCULM 1. Nat Commun. 3:752. https://doi.org/10.1038/ncomms1716.

Liu F et al. 2013. OsVPS9A functions cooperatively with OsRAB5A to regulate post-Golgi dense vesicle-mediated storage protein trafficking to the protein storage vacuole in rice endosperm cells. Mol Plant. 6:1918–1932. https://doi.org/10.1093/mp/sst081.

Liu X et al. 2019. Atlastin-1 regulates morphology and function of endoplasmic reticulum in dendrites. Nat Commun. 10:568. https://doi.org/10.1038/s41467-019-08478-6.

Livak KJ, Schmittgen TD. 2001. Analysis of relative gene expression data using real-time quantitative PCR and the $2^{-\Delta\Delta Ct}$ method. Methods. 25:402–408. https://doi.org/10.1006/meth.2001.1262

Moriya K et al. 2013. Protein N-myristoylation plays a critical role in the endoplasmic reticulum morphological change induced by overexpression of protein lunapark, an integral membrane protein of the endoplasmic reticulum. PLoS One. 8:e78235.

https://doi.org/10.1371/journal.pone.0078235.

Okamoto M et al. 2012. High-curvature domains of the ER are important for the organization of ER exit sites in *Saccharomyces cerevisiae*. J Cell Sci. 125:3412–3420. https://doi.org/10.1242/jcs.100065.

Orso G et al. 2009. Homotypic fusion of ER membranes requires the dynamin-like GTPase Atlastin. Nature. 460:978–983. https://doi.org/10.1038/nature08280.

Portela M et al. 2019. Oncogenic dependence of glioma cells on kish/TMEM167A regulation of vesicular trafficking. Glia. 67:404–417. https://doi.org/10.1002/glia.23551.

Ren Y et al. 2014. *GLUTELIN PRECURSOR ACCUMULATION3* encodes a regulator of post-Golgi vesicular traffic essential for vacuolar protein sorting in rice endosperm. Plant Cell. 26:410–425. https://doi.org/10.1105/tpc.113.121376.

Ren Y et al. 2020. *GPA5* encodes a Rab5a effector required for post-Golgi trafficking of rice storage proteins. Plant Cell. 32:758–777. https://doi.org/10.1105/tpc.19.00863.

Ren Y et al. 2022. Endomembrane-mediated storage protein trafficking in plants: Golgi-dependent or Golgi-independent? FEBS Lett. 596:2215–2230. https://doi.org/10.1002/1873-3468.14374.

Segura-Collar B et al. 2020. The EGFR-TMEM167A-p53 axis defines the aggressiveness of gliomas. Cancers. 12:E208. https://doi.org/10.3390/cancers12010208.

Shemesh T et al. 2014. A model for the generation and interconversion of ER morphologies. Proc Natl Acad Sci U S A. 111: E5243-5251. https://doi.org/10.1073/pnas.141999711.

Shi L et al. 2024. Dissecting the mechanism of atlastin-mediated homotypic membrane fusion at the single-molecule level. Nat Commun. 15:2488. https://doi.org/10.1038/s41467-024-46919-z.

Shibata Y et al. 2008. The reticulon and Dp1/Yop1p proteins form immobile oligomers in the tubular endoplasmic reticulum. J Bio Chem. 283:18892–18904. https://doi.org/10.1074/jbc.M800986200.

Shibata Y, Voeltz GK, Rapoport TA. 2006. Rough sheets and smooth tubules. Cell. 126:435–439. https://doi.org/10.1016/j.cell.2006.07.019.

Sparkes I et al. 2010. Five Arabidopsis reticulon isoforms share endoplasmic reticulum location, topology, and membrane-shaping properties. Plant Cell. 22:1333–1343. https://doi.org/10.1105/tpc.110.074385.

Sparkes I, Hawes C, Frigerio L. 2011. FrontiERs: movers and shapers of the higher plant cortical endoplasmic reticulum. Curr Opin Plant Biol. 14:658–665. https://doi.org/10.1016/j.pbi.2011.07.006.

Sun J, Movahed N, Zheng H. 2020. LUNAPARK is an E3 ligase that mediates degradation of ROOT HAIR DEFECTIVE3 to maintain a tubular ER network in *Arabidopsis*. Plant Cell. 32:2964–2978. https://doi.org/10.1105/tpc.18.00937.

Sun J, Zheng H. 2018. Efficient ER fusion requires a dimerization and a C-terminal tail mediated membrane anchoring of RHD3. Plant Physiol. 176:406–417. https://doi.org/10.1104/pp.17.01411.

Sun S, Tang X, Guo Y, Hu J. 2021. Endoplasmic reticulum composition and form: Proteins in and out. Curr Opin Cell Biol.71:1–6. https://doi.org/10.1016/j.ceb.2021.01.008.

Tolley N et al. 2010. Transmembrane domain length is responsible for the ability of a plant reticulon to shape endoplasmic reticulum tubules *in vivo*: ER tubule formation by a reticulon protein. Plant J. 64:411–418. https://doi.org/10.1111/j.1365-313X.2010.04337.x.

Vitale A, Boston RS. 2008. Endoplasmic reticulum quality control and the unfolded protein response: insights from plants. Traffic. 9:1581–1588. https://doi.org/10.1111/j.1600-0854.2008.00780.x.

Wang G et al. 2024. Release of a ubiquitin brake activates OsCERK1-triggered immunity in rice. Nature. 629:1158–1164. https://doi.org/10.1038/s41586-024-07418-9.

Wang J et al. 2021. Transcriptional activation and phosphorylation of OsCNGC9 confer enhanced chilling tolerance in rice. Mol Plant. 14:315–329. https://doi.org/10.1016/j.molp.2020.11.022.

Wang S, Tukachinsky H, Romano FB, Rapoport TA. 2016. Cooperation of the ER-shaping proteins atlastin, lunapark, and reticulons to generate a tubular membrane network. eLife. 5:e18605. https://doi.org/10.7554/eLife.18605.

Wang W et al. 2023. WeiTsing, a pericycle-expressed ion channel, safeguards the stele to confer clubroot resistance. Cell. 186:2656-2671. https://doi.org/10.1016/j.cell.2023.05.023.

Wang W, Zheng H. 2024. Arabidopsis reticulons inhibit ROOT HAIR DEFECTIVE3 to form a stable tubular endoplasmic reticulum network. Plant Physiol. 194:1431–1446. https://doi.org/10.1093/plphys/kiad574.

Wang Y et al. 2010. OsRab5a regulates endomembrane organization and storage protein trafficking in rice endosperm cells: OsRab5a controls storage protein trafficking. Plant J. 64:812–824. https://doi.org/10.1111/j.1365-313X.2010.04370.x.

Wang Y et al. 2016. *GOLGI TRANSPORT 1B* regulates protein export from the endoplasmic reticulum in rice endosperm cells. Plant Cell. 28:2850–2865. https://doi.org/10.1105/tpc.16.00717.

Wendler F et al. 2010. A genome-wide RNA interference screen identifies two novel components of the metazoan secretory pathway. EMBO J. 29:304–314. https://doi.org/10.1038/emboj.2009.350.

Westrate LM, Lee JE, Prinz WA, Voeltz GK. 2015. Form follows function: the importance of endoplasmic reticulum shape. Annu Rev Biochem. 84:791–811. https://doi.org/10.1146/annurev-biochem-072711-163501.

Yan L et al. 2015. Structures of the yeast dynamin-like GTPase Sey1p provide insight into homotypic ER fusion. J Cell Biol. 210:961–972. https://doi.org/10.1083/jcb.201502078.

Zhang M et al. 2013. ROOT HAIR DEFECTIVE3 family of dynamin-like GTPases mediates homotypic endoplasmic reticulum fusion and is essential for Arabidopsis development. Plant Physiol. 163:713–720. https://doi.org/10.1104/pp.113.224501.

Zhao Y, Zhang T, Huo H, Ye Y, Liu Y. 2016. Lunapark is a component of a ubiquitin ligase complex localized to the endoplasmic reticulum three-way junctions. J Biol Chem. 291:18252–18262. https://doi.org/10.1074/jbc.M116.737783

Zheng H, Chen J. 2011. Emerging aspects of ER organization in root hair tip growth: lessons from RHD3 and atlastin. Plant Signaling Behav. 6:1710–1713. https://doi.org/10.4161/psb.6.11.17477.

Zheng H, Kunst L, Hawes C, Moore I. 2004. A GFP-based assay reveals a role for RHD3 in transport between the endoplasmic reticulum and Golgi apparatus. Plant J. 37:398–414. https://doi.org/10.1046/j.1365-313X.2003.01969.x.

Zhou X et al. 2019. Reciprocal regulation between lunapark and atlastin facilitates ER three-way junction formation. Protein Cell. 10:510–525. https://doi.org/10.1007/s13238-018-0595-7.

Zhu J et al. 2019. OsNHX5-mediated pH homeostasis is required for post-Golgi trafficking of seed storage proteins in rice endosperm cells. BMC Plant Biol. 19:295. https://doi.org/10.1186/s12870-019-1911-y.

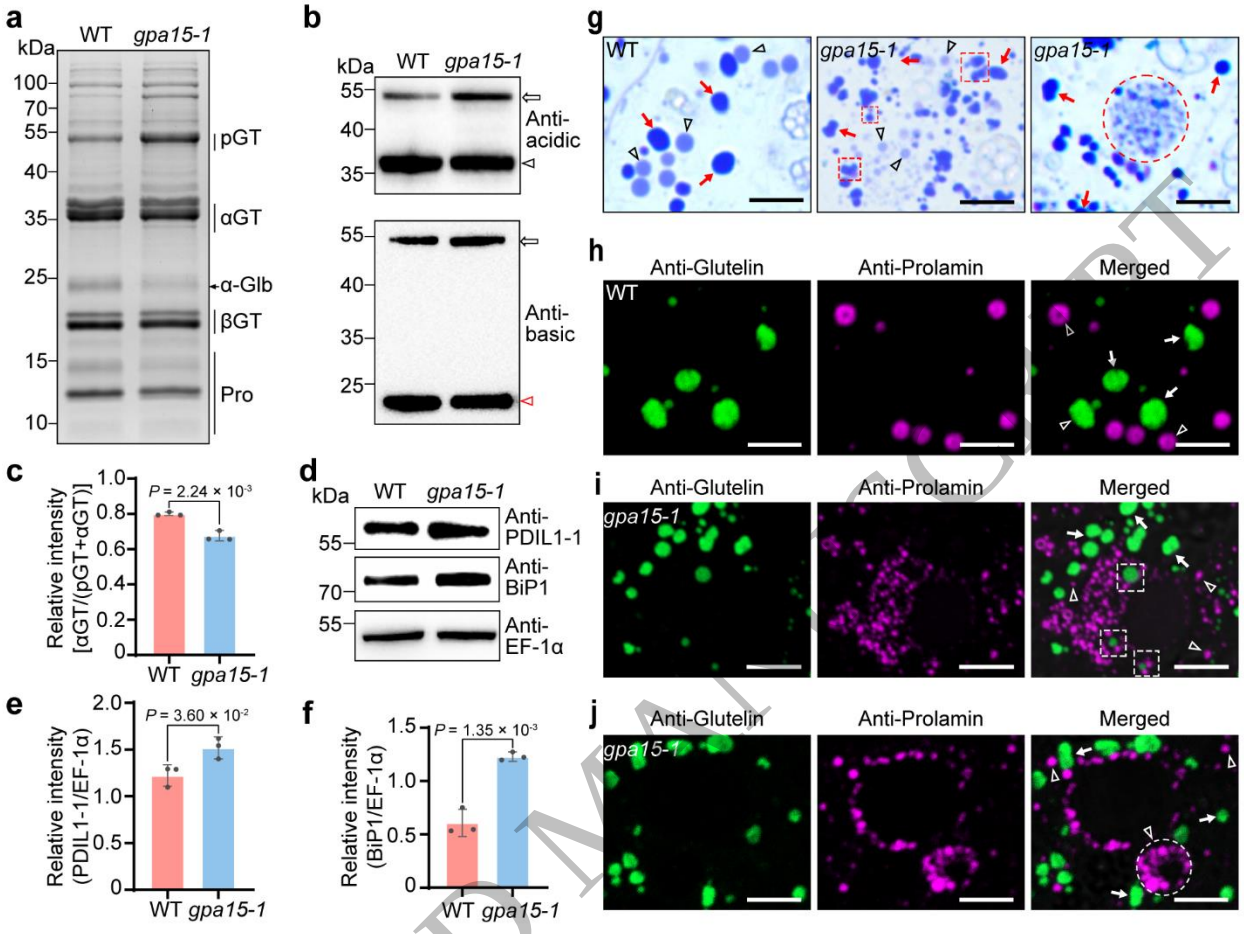

Fig. 1: Phenotypic characterization of the *gpa15-1* mutant.

a) Total seed storage protein profile of wild-type (WT) and *gpa15-1* mature dry seeds on an SDS-PAGE gel stained with Coomassie Brilliant Blue (CBB). Molecular weight markers are shown on the left (kDa). Note the overaccumulation of unprocessed glutelin precursors in *gpa15-1*. pGT, unprocessed glutelin precursors; αGT, mature glutelin acidic subunits; α-Glb, 26-kDa α-globulin; βGT, mature glutelin basic subunits; Pro, prolamins. **b)** Immunoblotting analysis of storage proteins with anti-glutelin mature acidic subunits and anti-basic subunits. Arrows and arrowheads indicate the unprocessed glutelin precursors and mature glutelin subunits (black for acidic subunits, red for basic subunits), respectively. **c)** Quantification of relative glutelin precursor processing efficiency in **(b)**, calculated as αGT / (pGT + αGT). Values are means ± SD. **d)** Immunoblotting analysis of dry seeds with anti-molecular chaperone antibodies (PDIL1-1 and BiP1). EF-1α was used as a loading control in **(b)** and **(d)**. **e)** and **f)** Quantification of molecular chaperone proteins PDIL1-1 and BiP1 in **(d)**. Note the increased abundance of both chaperones in *gpa15-1*. Values are means ± SD. **g)** CBB-stained semi-thin sections of developing endosperm of WT and *gpa15-1* at 12 days after flowering (DAF). Red arrows and black arrowheads indicate the dark-stained glutelin-containing PBIIs with

irregular shape and the light-stained round-shaped prolamin-containing PBIs in WT and *gpa15-1*, respectively. Red dotted lines outline two types of novel structures observed specifically in *gpa15-1*. Scale bars, 5 μm. **h)** to **j)** Immunofluorescence microscopy images of storage proteins in WT and *gpa15-1* seeds. Secondary antibodies conjugated with Alexa Fluor 488 (green) and Alexa Fluor 555 (magenta) were used to trace antigens recognized by anti-glutelin and anti-prolamin antibodies, respectively. White arrows and arrowheads indicate the glutelin-containing PBIIs with irregular shape and the round-shaped prolamin-containing PBIs in WT and *gpa15-1*, respectively. White dotted lines outline two types of novel structures in *gpa15-1*. Scale bars, 5 μm. In **(c)**, **(e)**, and **(f)**, statistical analysis was performed by a two-tailed Student's *t*-test ($n = 3$).

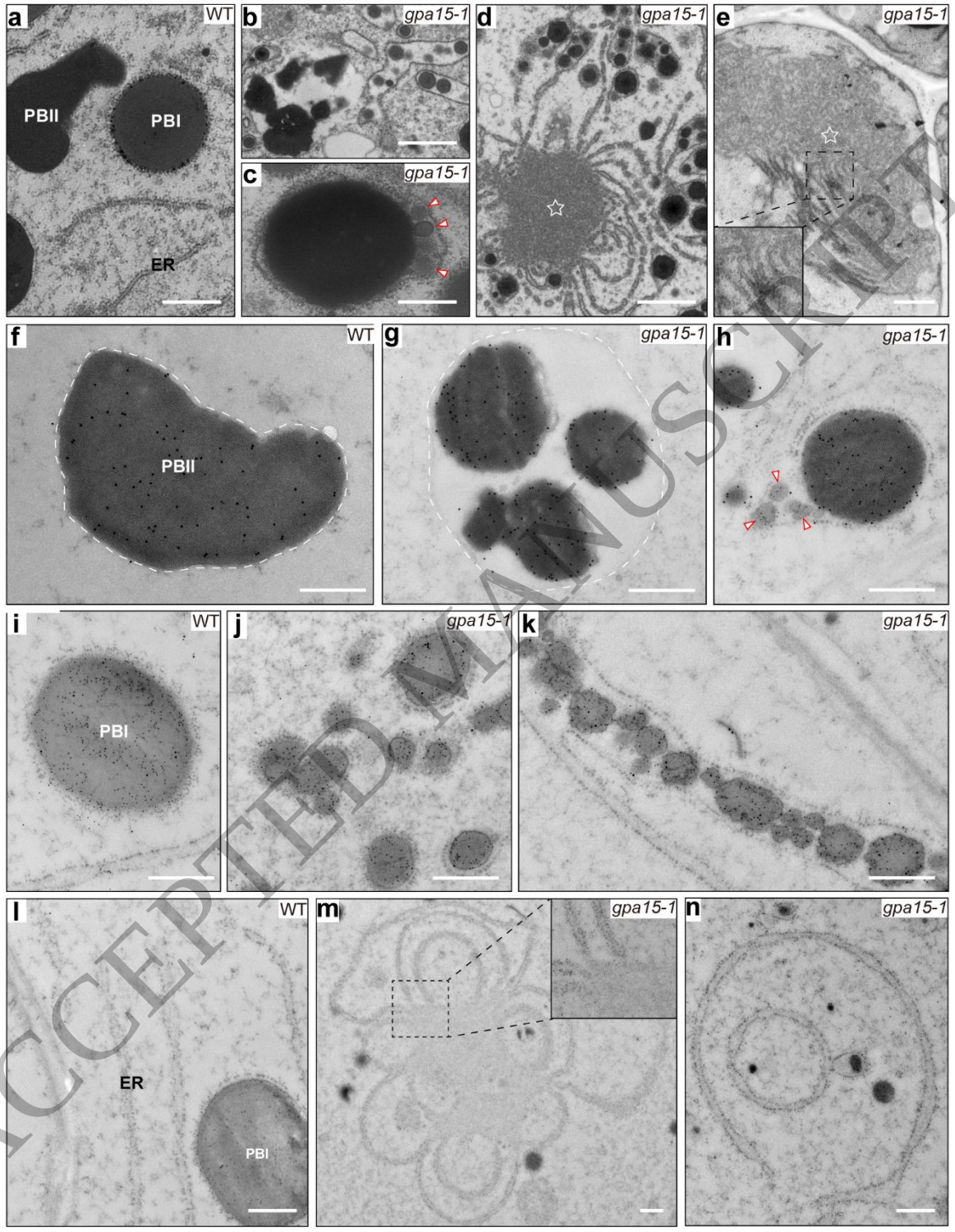

Fig. 2: Ultrastructure of subaleurone cells of developing endosperm in wild type and *gpa15-1*.

Ultrathin sections were prepared from wild-type (WT) or *gpa15-1* developing subaleurone cells at 12 days after flowering (DAF), followed by double-immunogold labelling with anti-glutelin (15-nm gold) and anti-prolamin (10-nm gold) antibodies **(e)** to **(m)**.
a) Typical spherical PBIs and irregular PBII together with the ER in the WT. Scale bar, 1 μm. **b)** Aberrant PBIs and incompletely filled PBIIs in *gpa15-1*. Scale bars, 1 μm. **c)** Compound PBs observed specifically in *gpa15-1*. Red arrowheads indicate several small round proteins. Scale bars, 500 nm. **d)** and **e)**, Large ER-associated aggregates are readily observed in *gpa15-1*. The inset in **(e)** is the enlarged image of the corresponding boxed area. The large aggregates represented by stars are actually clusters of dense ER tubules. Scale bars, 1 μm. **f)** and **g)**, PBIIs in WT **(f)** and *gpa15-1* **(g)**. The dashed line indicates the peripheral outline of the protein body. Scale bars, 500 nm. **h)** The compound PB contains a glutelin core and a prolamin periphery. Red arrowheads represent the prolamin proteins. Scale bars, 500 nm. **i)** to **k)** Spherical PBIs in the WT and scattered prolamin aggregates in *gpa15-1*. Scale bars, 500 nm. **l)** to **n)** ER morphology in WT and *gpa15-1*. Scale bars, 500 nm.

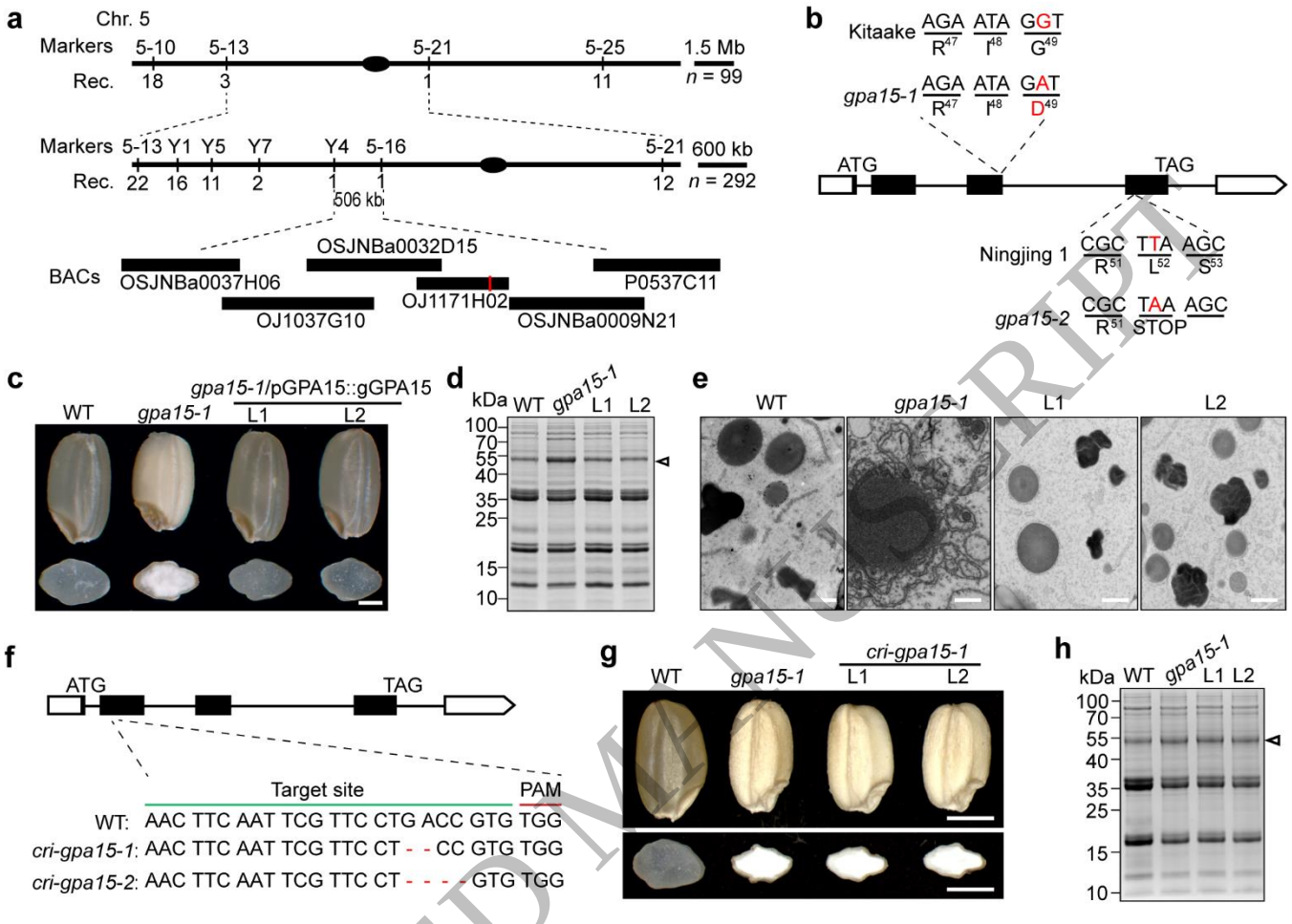

Fig. 3: Map-based cloning of *GPA15*.

a) Fine mapping of the *GPA15* locus. The molecular markers and the numbers of recombinants are shown. The red line in BAC OJ1171H02 indicates the localization of the causal gene. **b)** Gene structure and the mutation site in *Os05g0251500*. *Os05g0251500* comprises four exons (closed boxes) and three introns (lines). ATG and TGA represent start and stop codons, respectively. Missense and nonsense mutations occurred in *gpa15-1* and *gpa15-2*, respectively. **c)** to **e)** A 6.4-kb wild-type genomic fragment of *GPA15* rescues the phenotypic defects of *gpa15-1*, including grain appearance **(c)**, total seed storage protein profile resolved on a CBB-stained SDS-PAGE gel **(d)**, and storage protein trafficking defects **(e)**. L1 and L2 represent two independent T1 transgenic lines. Scale bars, 1 mm in **c**, 1 μm in **e**. **f)** Sketch map of the mutation sites in the *GPA15* knockout lines. The knockout site was designed by CRISPR-P (CRISPR-P v2.0). PAM, protospacer adjacent motif. White boxes indicate untranslated regions (UTRs), black boxes indicate exons, and lines indicate introns. **g)** and **h)** Knockout of *GPA15* results in phenotypic defects similar to those of *gpa15-1*,

including grain appearance **(g)** and total seed protein profile **(h)**. Arrowhead indicates the glutelin precursors. Scale bars, 2 mm in **(g)**.

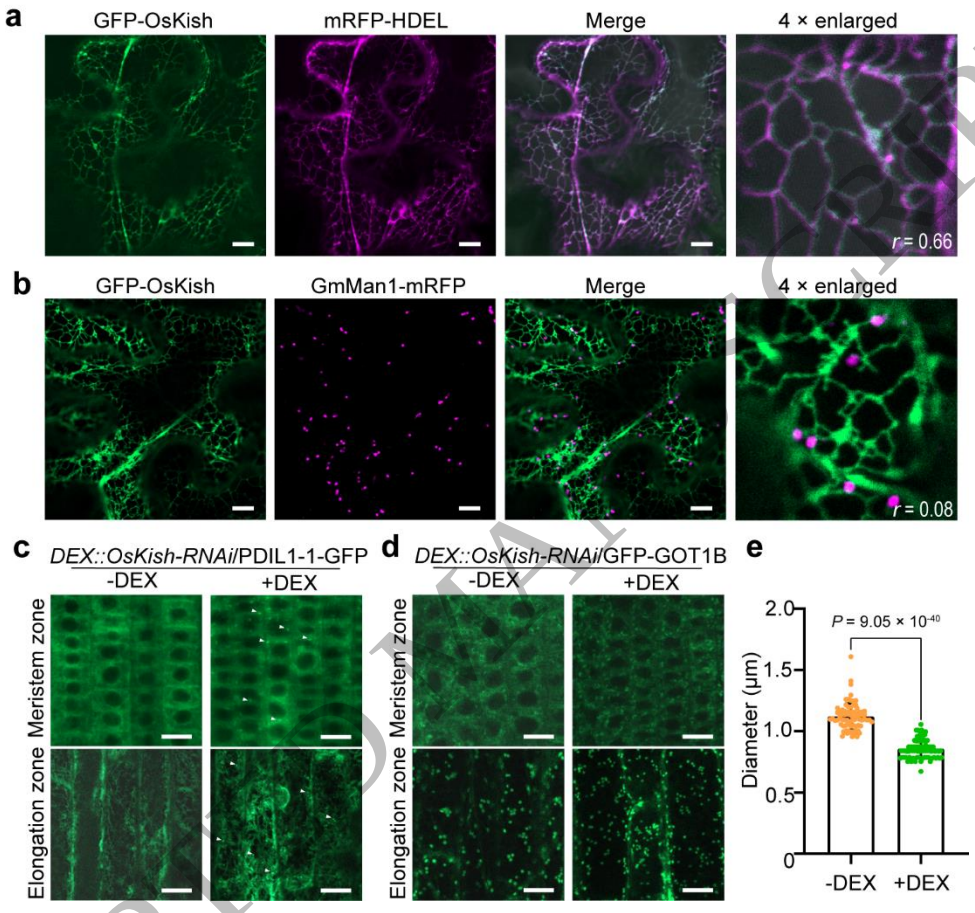

Fig 4. OsKish is essential for maintaining the normal ER function.

a) and **b)** Confocal microscopic images showing that GFP-OsKish substantially colocalizes with the ER marker (mRFP-HDEL) but not with the Golgi marker (GmMan1-mRFP). Pearson's correlation coefficients (r_s) are shown in the right panel. Scale Bars, 10 μm. **c)** Subcellular location patterns of PDIL1-1-GFP in *DEX::OsKish-RNAi*/PDIL1-1-GFP root tip cells. White arrowheads indicate punctate fluorescence signals. Scale Bars, 10 μm. **d)** Subcellular location patterns of GFP-GOT1B in *DEX::OsKish-RNAi*/GFP-GOT1B root tip cells. Scale Bars, 10 μm. All transgenic lines in **(c)** and **(d)** were generated in the DEX-inducible *OsKish* RNAi plant background. Ten-day-old seedlings were treated with or without DEX for 6 h in the dark, followed by examination of fluorescence in the meristematic and elongation zones of root tip cells. **e)** Statistical analysis of the diameters of

fluorescence puncta in **(d)**. Values are individual data points and means ± SD. Statistical analysis was performed by a two-tailed Student's *t*-test (n = 80).

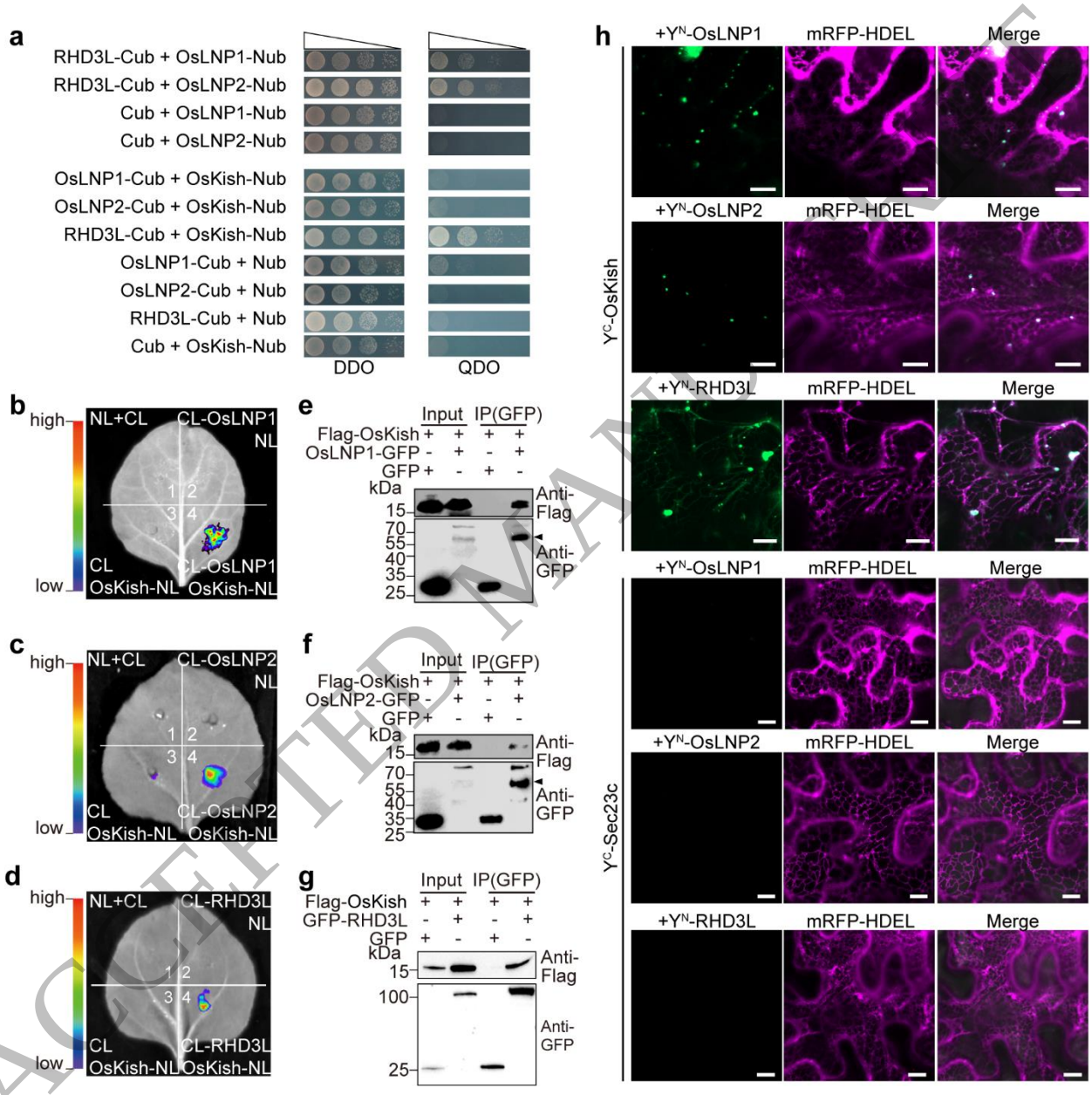

Fig. 5: OsKish physically interacts with OsLNPs and RHD3L.

a) Y2H assays showing the interactions between OsKish, OsLNPs, and RHD3L. DDO, SD/-Trp/-Leu; QDO, SD/-Trp/-Leu/-His/-Ade. **b)** to **d)** LCI assays confirming that OsKish specifically interacts with OsLNPs and RHD3L in leaf cells of *N. benthamiana*. Colored scale bars indicate the luminescence

intensity in counts per second (cps). **e)** to **g)** Co-IP assays verifying the interactions of OsKish with OsLNPs and RHD3L. Total protein extracts were immunoprecipitated with anti-GFP magnetic beads, followed by immunoblotting with anti-Flag or anti-GFP antibodies. Input lysates (10% of total protein) were included and analyzed in parallel to verify comparable protein expression levels across samples. IP, immunoprecipitation. **h)** BiFC assays showing that OsKish interacts with OsLNPs and RHD3L in the ER. OsLNPs and RHD3L do not interact with Sec23c (negative control). Scale bars, 10 μm.

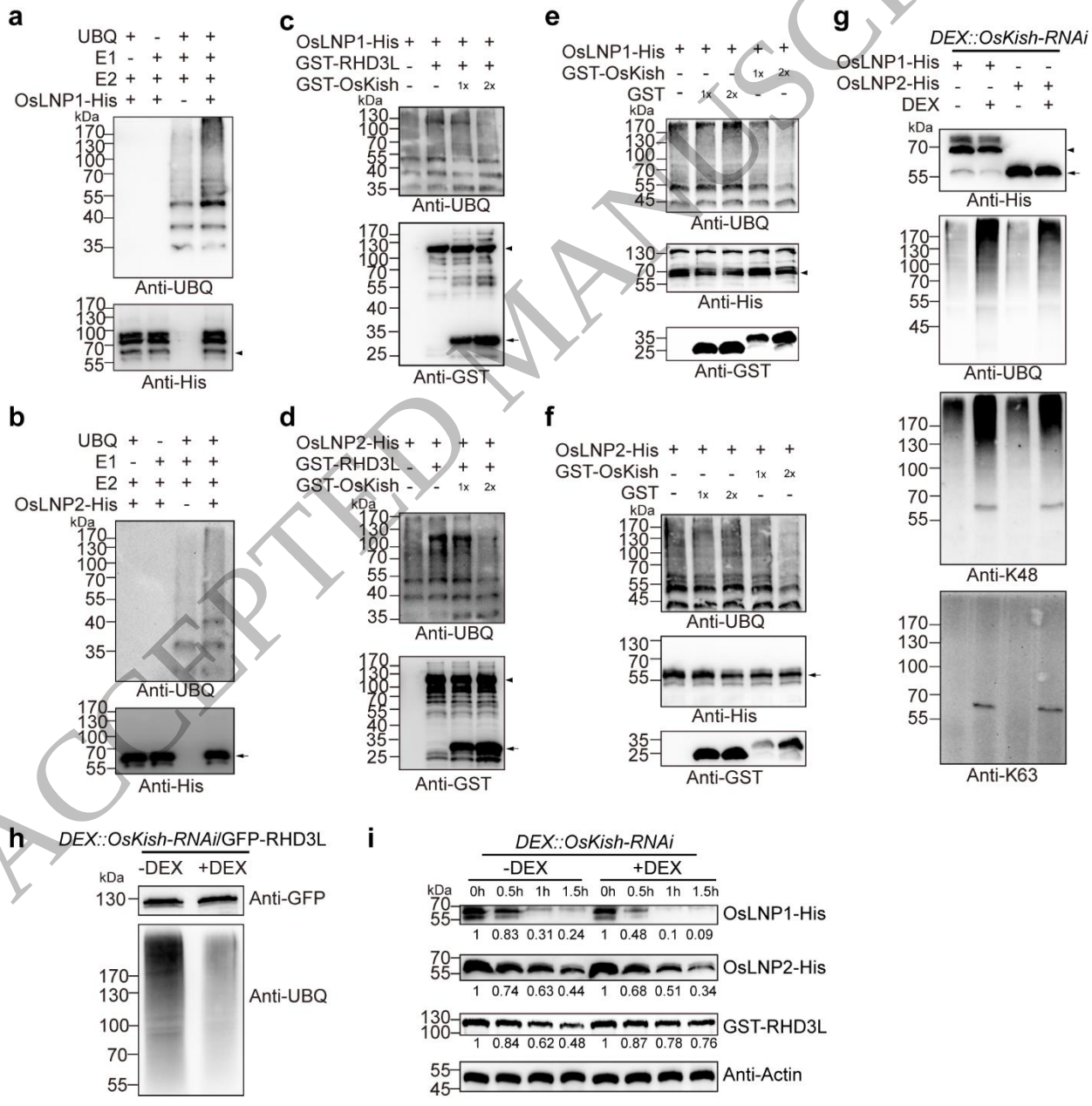

Fig. 6: The auto-ubiquitination and degradation of OsLNPs by OsKish

a) and **b)** The self-activation of OsLNP1-His and OsLNP2-His as E3 ligases in the presence of an E1 ubiquitin-activating enzyme, an E2 ubiquitin-conjugating enzyme, and ubiquitin (UBQ). The arrowhead indicates the OsLNP1-His band, while the arrow indicates the OsLNP2-His band. **c)** and **d)** The ubiquitination of RHD3L by OsLNP1 and OsLNP2 is suppressed in the presence of OsKish. The arrowhead indicates the GST-RHD3L band, while the arrow indicates the GST-OsKish band. Note that enhanced smear signals detected by the anti-GST antibody in the presence of GST-OsKish are attributed to the GST-OsKish. **e)** and **f)** Reduction of the auto-ubiquitination activity of OsLNP1-His and OsLNP2-His by OsKish *in vitro*. The arrowhead indicates the OsLNP1-His band, while the arrow indicates the OsLNP2-His band. **g)** Increased auto-ubiquitination of OsLNP1-His and OsLNP2-His in the semi-*in vitro* ubiquitination assay. Total proteins were extracted from *DEX::OsKish-RNAi* seedlings treated with or without DEX. The samples immunoblotted with anti-His antibody were used as a loading control. Anti-K48 and anti-K63 antibodies were used to detect K48- and K63-linked ubiquitin chains, respectively. The arrowhead indicates the OsLNP1-His band, while the arrow indicates the OsLNP2-His band. **h)** Decreased ubiquitination of RHD3L in the *in vitro* ubiquitination assay. Total proteins were extracted from *DEX::OsKish-RNAi/GFP-RHD3L* seedlings treated with or without DEX. The samples immunoblotted with anti-GFP antibody were used as a loading control. **i)** OsLNP1-His and OsLNP2-His are degraded faster, while GST-RHD3L is degraded slower in *DEX::OsKish-RNAi* seedlings after DEX induction in the cell-free degradation assay. Total proteins were extracted from *DEX::OsKish-RNAi* seedlings treated with or without DEX. Band intensities were quantified relative to the protein amount at 0 h and are indicated underneath the blot. Anti-actin antibody was used as a loading control. Three independent experiments were performed with similar results.

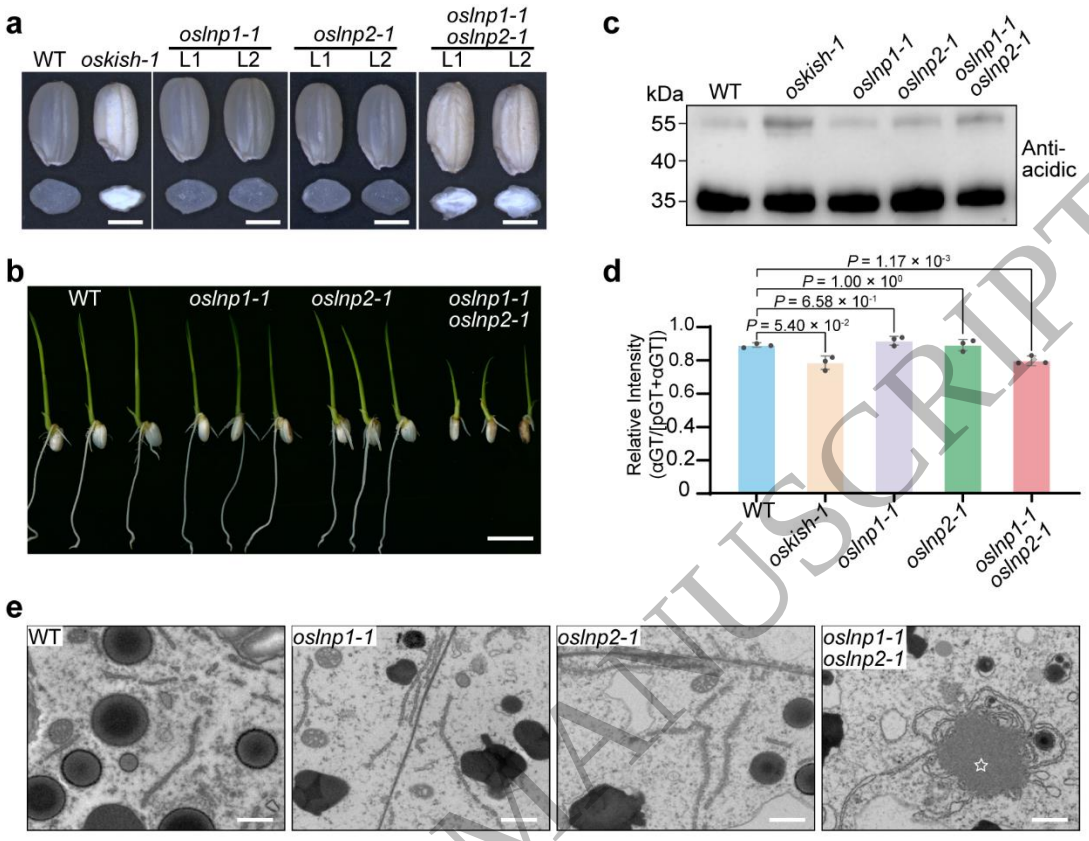

Fig. 7: Phenotypic characterization of the *oslnp1-1* single mutant, the *oslnp2-1* single mutant, and the *oslnp1-1 oslnp2-1* double mutant.

a) The grain appearance of the wild type (WT), the *oskish-1* mutant, the *oslnp1-1* single mutant, the *oslnp2-1* single mutant, and the *oslnp1-1 oslnp2-1* double mutant. Scale bars, 2 mm. **b)** Images of the WT, the *oskish-1* mutant, the *oslnp1-1* single mutant, the *oslnp2-1* single mutant, and the *oslnp1-1 oslnp2-1* double mutant seedlings grown for 7 d on half-strength MS medium. Scale bar, 1 cm. **c)** Immunoblotting analysis of dry seeds of the WT, the *oskish-1* mutant, the *oslnp1-1* single mutant, the *oslnp2-1* single mutant, and the *oslnp1-1 oslnp2-1* double mutant with anti-glutelin mature acidic subunit antibodies. **d)** Quantification of immunoblotting data for glutelin processing efficiency in **(c)**. Values are means ± SD. Statistical analysis was performed using one-way ANOVA followed by Dunnett's multiple comparisons test; error bars represent standard deviations. **e)** Ultrastructure of subaleurone cells in the developing endosperm of the WT, the *oskish-1* mutant, the *oslnp1-1* single mutant, the *oslnp2-1* single mutant, and the *oslnp1-1 oslnp2-1* double mutant. The ER aggregate is indicated by a star. Scale bars, 1 μm.

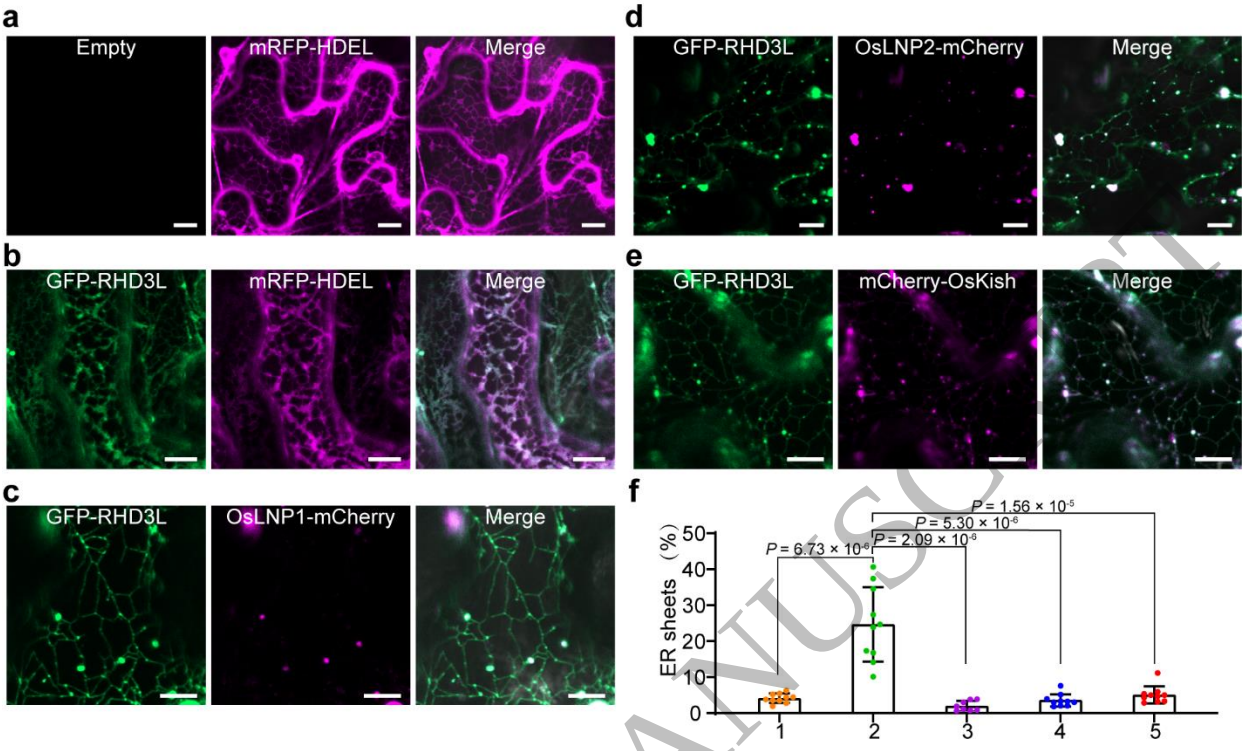

Figure 8. *OsKish* overexpression inhibits RHD3L-mediated membrane fusion.

a) to **e)** Representative images of five different transient expression experiments in epidermal cells of *N. benthamiana* leaves. **(a)** mRFP-HDEL alone; **(b)** GFP-RHD3L and mRFP-HDEL; **(c)** GFP-RHD3L and OsLNP1-mCherry; **(d)** GFP-RHD3L and OsLNP2-mCherry; **(e)** GFP-RHD3L and mCherry-OsKish. Scale bars, 10 μm. **f)** Quantification of ER sheets defined by ImageJ in **(a)** to **(e)** (columns 1 to 5). At least 10 independent cells were analyzed for each combination. Statistical analysis was performed using one-way ANOVA followed by Tukey's test; error bars represent standard deviations.

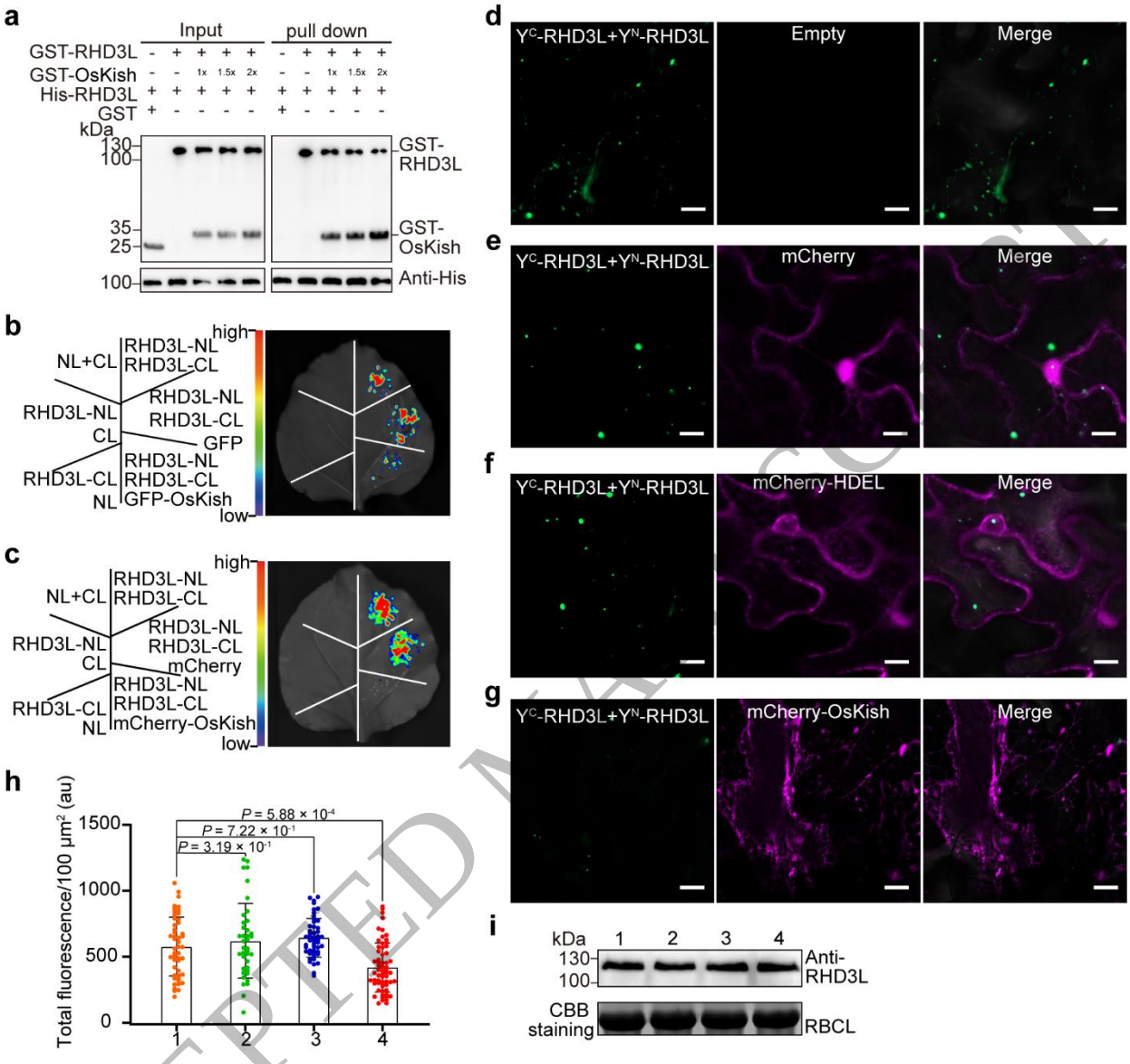

Fig. 9: *OsKish* overexpression disrupts the oligomerization of RHD3L.

a) Competitive pull-down assays demonstrating that OsKish disrupts the RHD3L self-interaction. **b)** and **c)** LCI assays verifying the self-interaction of RHD3L in the presence of GFP and GFP-OsKish **(b)** as well as mCherry and mCherry-OsKish **(c)** in leaf cells of *N. benthamiana*. Colored scale bar indicates the luminescence intensity. CL, C terminus of LUC; NL, N terminus of LUC. **d)** to **g)** BiFC assays verifying the self-interaction of RHD3L while coexpressed with empty **(d)**, mCherry **(e)**, mCherry-HDEL **(f)**, and mCherry-OsKish **(g)**. Scale bars, 10 μm. **h)** Quantification of the BiFC fluorescence (arbitrary units) of all fluorescent spots in fields of view of identical size, randomly selected from cells expressing empty (column 1), mCherry (column 2), mCherry-HDEL (column 3), and mCherry-OsKish (column 4). At least 20 cells were analyzed for each combination. Statistical

analysis was performed using one-way ANOVA followed by Tukey's test: error bars represent standard deviations. **i)** The abundance of RHD3L proteins was detected by immunoblotting with anti-RHD3L antibodies. CBB-stained RBCL bands were used as the internal reference for total protein loading.